Exploring [CII] Haloes and Quasar Environments in and near the Epoch of Reionization

TESIS PRESENTADA POR

Trystan Scott Lambert

A LA

FACULTAD DE INGENIERÍA Y CIENCIAS
INSTITUTO DE ESTUDIOS ASTROFÍSICOS

Para optar al Grado de Doctor en Astrofísicos

Profesor guía: Roberto J. Assef Trebilcock

UNIVERSIDAD DIEGO PORTALES

Santiago, Chile
2023

Exploring [CII] Haloes and Quasar Environments in and near the Epoch of Reionization

TESIS PRESENTADA POR

Trystan Scott Lambert

A LA

FACULTAD DE INGENIERÍA Y CIENCIAS
INSTITUTO DE ESTUDIOS ASTROFÍSICOS

Para optar al Grado de Doctor en Astrofísicos

Profesor guía: Roberto J. Assef

UNIVERSIDAD DIEGO PORTALES

Santiago, Chile
2023

Exploring [CII] Haloes and Quasar Environments in and near the Epoch of Reionization

by

Trystan Scott Lambert
Instituto de Estudios Astrofísicos
Facultad de Ingeniería y Ciencias
Universidad Diego Portales

Supervisor:

Roberto J. Assef
Instituto de Estudios Astrofísicos
Facultad de Ingeniería y Ciencias
Universidad Diego Portales

Examiners' Committee

Name and affiliation	**Signature**
Prof. Manuel Aravena Instituto de Estudios Astrofísicos Facultad de Ingeniería y Ciencias Universidad Diego Portales	....
Prof. Chiara Mazzucchelli Instituto de Estudios Astrofísicos Facultad de Ingeniería y Ciencias Universidad Diego Portales	....
Prof. Lucia Guaita Departamento de Ciencias Fisicas Universidad Andres Bello	....
Prof. Peter Eisenhardt Jet Propulsion Laboratory California Institute of Technology	....

Date: December 2023

Dedication

This thesis is dedicated to all the people who left me at different stages of my academic journey:

To Garreth, just before undergrad. He taught me that that very few things in life are more precious than a good friend, and those true friendships need to be treasured and protected.

To “Chicken” Granny, At the end of undergrad. She taught me that I would always be loved, and if I could get through that night, I could get through anything.

To “Cottage” Granny, the next week. She taught me that no matter how many hours you give to your work, it will never give you more than what your family does.

To Uncle Nige, during my Ph.D. He taught me to value the people you have around you now, because they’re not guaranteed to be here tomorrow.

I miss them all dearly, more than words could ever say. It’s not the same without you here.

Acknowledgements

"If I have seen further it is by standing on the shoulders of Giants" is the famous quote by Isaac Newton, and I feel this is particularly true in my case. I have a great many people to thank, not just during my Ph.D., but on this whole scientific journey.

I first want to thank my Supervisor, Roberto Assef, for guiding me through this work; not only academically, but emotionally as well. His expertise and breath of knowledge, as well as consistent good-temperdness, have been inspiring.

I also thank my co–supervisor Manuel Aravena who was an essential part when I first started this Ph.D. He has been exceptionally kind and thoughtful throughout and the first part of this work would have been impossible without him.

I'd like to thank Jorge Gonzalez-Lopez for his mastery of ALMA and all things interferometry based. I could never have written the first paper without his help.

Thank you to Ana and Pedro, who welcomed me into UDP with open arms, and whose generosity, selfless, and kindness has been inspiring.

To Dejene for being a dear friend during this last year and for exuding the african spirit.

Thank you to Michele and Camila who organized the viewings for the rugby world cup matches; those were the times I felt the most at home. Thank you to the Springboks for giving me hope when I needed it the most.

Thank you to Prof. Thomas Jarrett, Prof. Renée Kraan-Korteweg, and Prof. Lucas Macri, who all played a critical role in getting me into astronomy, and have all been my academic heroes throughout my career.

Thank you to all my family who are to many to mention. They have always given me an the utmost support and encouragement, even if they never understood what I did. I love them all very much. In particular thank you to my parents. My dad has always helped me try find the humor in every situation. My mom has been the most important rock in my life, always keeping me anchored, and has been my greatest supporter.

Lastly, I want to thank my partner, Nadia, without whom none of this would have been possible. Thank you for patiently listening to all my complaints and showing me what it means to be a supportive partner. No matter how difficult things get I remember just how lucky I am that you came into my life.

And to everyone else that wasn't mentioned here, but who have been there for me all the time. I have infinite gratitude for everyone in my life.

Trystan Scott Lambert
Instituto de Estudios Astrofísicos
Facultad de Ingeniería y Ciencias
Universidad Diego Portales
Santiago, Chile
December 2023

Abstract

Studying galaxies' ISM and environments at high redshifts is an essential component to study galaxy evolution. With this in mind, this thesis is divided into two main projects, the first of which involves studying the ISM of a "normal", main-sequence galaxy at $z = 5.25$

High-redshift observations are often biased towards massive and bright galaxies that are not necessarily representative of the full population. In order to accurately study galaxy evolution and mass assembly at these redshifts, observations of "normal" main sequence galaxies are required. Here we present Atacama Large Millimeter/Submillimeter Array (ALMA) 0.3 arcsec resolution observations of the [C II] emission line at 158 μm of HZ7, a main sequence galaxy at $z = 5.25$. Comparing to archival rest-frame UV observations taken by the Hubble Space Telescope (HST), we find strong evidence of the existence of extended [C II] emission, which we estimate to be twice the size of the rest-frame UV emission, yielding one of the first high-redshift objects where a clear signature of a [C II] "Halo" has been detected to date. For a matched Sérsic profile with $n = 1$, we measured a [C II] effective radius of 0.50 ± 0.04 arcsec (3.07 ± 0.25 kpc) and an average rest-frame UV effective radius of 0.2 ± 0.04 arcsec (1.48 ± 0.16 kpc). The [C II] morphology and kinematics of the system suggest a merging event resulting in a non-rotating disc system. This event could be responsible for the extended [CII] emission. Alternatively, some potential obscured emission could also explain the [C II] to UV size ratio. These results contribute to the growing consensus with respect to the existence of extended [C II] emission around galaxies.

The second project focuses identifying Lyman-alpha emitters around a high-redshift quasar. High-redshift quasars are thought to live in the most dense regions of space which should be made evident by an overdensity of galaxies around them. However, campaigns to identify these overdensities through the search of Lyman Break Galaxies (LBGs), with broad photometric bands, and Lyman α emitters (LAEs), with narrow photometric bands, have had mixed results. These may be explained by either the small field of view of some of the experiments, the broad redshift ranges targeted by LBG searches, and by the inherent large uncertainty of quasar redshifts estimated from UV emission lines, which makes it difficult to place the Ly-α emission line within a narrowband filter. Here we present a three square degree search ($\sim$ 1000 pMpc) for LAEs around the $z = 6.9$ quasar VIK J2348–3054 using the Dark Energy CAMera (DECam), housed on the 4m Blanco telescope, finding 38. The systemic redshift of VIK J2348–3054 is known from ALMA [CII] observations and place the Ly-α emission line of companions within the NB964 narrowband of DECam. This is the largest field of view LAE search around a $z > 6$ quasar conducted to date. We find that this field is

~ 10 times more overdense when compared to the Chandra Deep-Field South, observed previously with the same instrumental setup. This is strong evidence that J2348 resides in an overdensity of LAEs over several Mpc. Surprisingly, we find a lack of LAEs within 5 pMpc of the quasar and take this to be evidence of the quasar suppressing star formation in its immediate vicinity. This result highlights the importance of performing these kinds of overdensity searches over large areas to properly assess the density of those regions of the Universe.

Table of Contents

List of Figures

List of Tables

Chapter 1

Introduction

Galaxies in the local universe have many different shapes, structures, and sizes. Some are enormous elliptical galaxies, who no longer form stars. Others are young, bright galaxies with immaculate spiral and bar structures, brimming with young stars. At the same time "dead" spiral galaxies, and star forming ellipticals are exceedingly rare; despite the large variety in galaxy morphologies, there appears to be a distinctive trend, implying some kind of evolution. How this evolutionary trend comes about is a very difficult question to answer and requires investigating different physical processes across cosmic time. If we want to know how galaxies evolve then it is natural to see how their properties change with time (i.e, with redshift).

Many studies, most famously Madau & Dickinson (2014a), have shown that some galaxy properties have a relationship with redshift. Figure 1.1 (adapted from their work) shows the star formation rates (SFRs) of galaxies as a function of redshift, derived from various infrared (IR) and far ultraviolet (FUV) observations. There is an obvious increase in SFR from the local universe towards earlier times that eventually peaks at $z = 2$ and then decreases towards higher redshifts. This peak at $z = 2$ has become known as "cosmic noon". And SFR is not the only property that follows this trend. SFR density, and supermassive black hole accretion rates similarly peak at cosmic noon (Shapley, 2011, Vito et al., 2018).

Why would these properties (and maybe others) depend on redshift? To answer this, it is important to realize that galaxies do not live in a vacuum and are both influenced and influence their environments. Understanding the relationship between how galaxies shape their surroundings, and how their surroundings influence their properties is an essential aspect of studying galaxy evolution. For example, there exists a co-evolution between black hole accretion rate and SFR, simply because the amount of available gas for both of these processes increases towards higher redshifts (Carraro et al., 2020). At

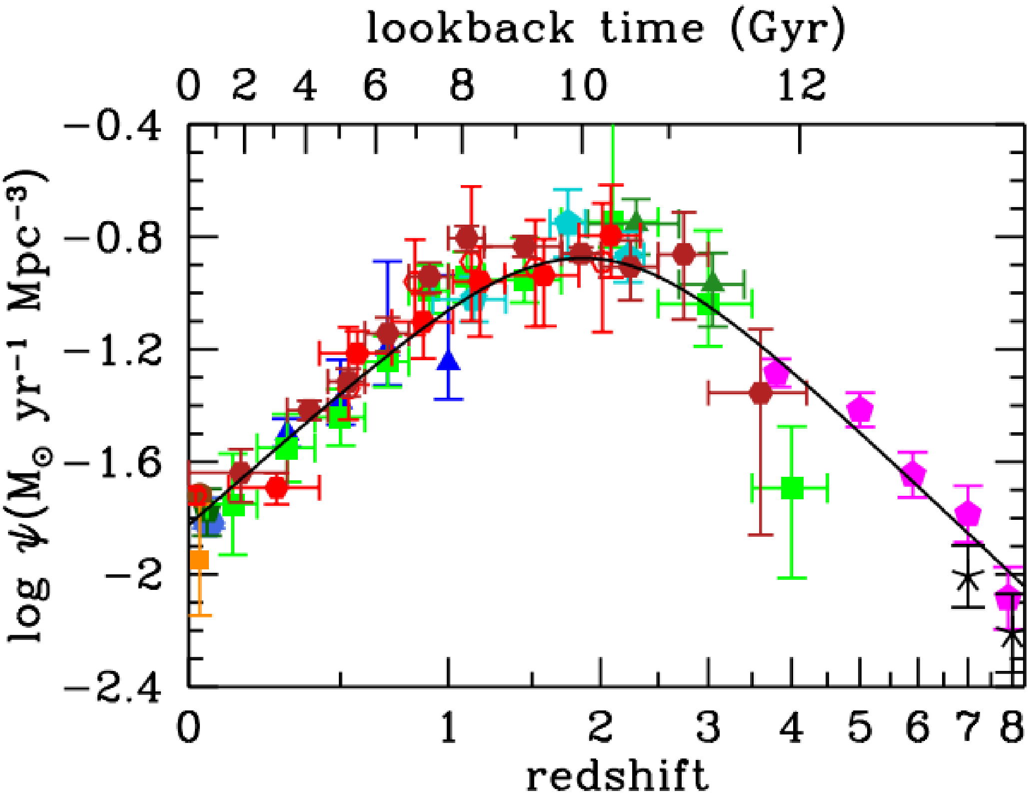

Figure 1.1: Figure 9. from Madau & Dickinson (2014a) showing the relationship between star formation rate (SFR) and redshift. Points are from various IF and FUV studies which have been converted into SFRs.

the same time this gas has to be dense enough to form galaxies and black holes, which is a competing effect that gets harder at higher redshifts, explaining the decline after $z > 2$. This highlights the need for higher redshift studies, in order to create a complete picture of how galaxies evolve over time, pushing the well established trend from $z = 0$ to $z = 2$ to higher redshifts, even up $z > 5$.

We can therefore tackle the problem of studying galaxy evolution in two different, but intimately related ways: first, by tracing the flow of baryons into and out of high-z galaxies, i.e., the stuff that makes up galaxies; and second, by exploring the environments around high-z galaxies.

This thesis focuses on these two methods. In particular: by studying the Inter Stellar Medium (ISM), i.e., the fuel for star formation, of a “normal” galaxy at $z = 5.25$, using [CII] line observations from the Atacama Large Millimeter Array (ALMA). These galaxies are akin to the kinds of galaxies we expect are the primary sources of reionization—the period in the early universe ($z > 5.3$; Bosman et al., 2022), called the epoch of reionization (EoR), where galaxies and stars where ionizing the neutral gas. And by studying the environment around a quasar close to the EoR ($z \approx 6.9$) via looking for Lyman-α

emitters (LAEs) as tracers of overdensities, allowing us to probe the hierarchical formation theory that these sources should be found in the densest dark-matter haloes in the early universe.

1.1 Studying galaxy evolution using the building blocks of star formation.

One important way in which galaxies interact with their environment is through their baryon cycles, i.e., the movement of baryons into, and out of the galaxy (Faisst et al., 2022). The chemical enrichment of both a galaxy's interstellar medium (ISM) and its intergalactic medium (IGM) can be achieved through galaxy-galaxy interactions, inflows, and outflows (Ginolfi et al., 2020a, Hani et al., 2018, Nelson et al., 2015, Pallottini et al., 2014).

Optical, UV, and Far infrared studies of low-z galaxies ($z < 3$), have resulted in a solid picture of how galaxies evolve (Faisst et al., 2022) and one of the most important properties to track through cosmic time to do this, is star formation. As discussed earlier, we know that the SFR density peaked at $z = 2$—the so called "cosmic noon"—and on average, it appears that galaxies were more star forming early on in the history of the Universe with far fewer quiescent galaxies at higher redshifts (Faisst et al., 2022). Previously this trend was thought to be due to an increase in mergers in the early universe, and while it is true that mergers are more frequent with increasing redshift (Gottlöber et al., 2001, Kampczyk et al., 2013, Rodriguez-Gomez et al., 2015), recent research has shown that the main reason for the increase in star formation towards cosmic noon is due to the increased availability of gas (Daddi et al., 2007, Faisst et al., 2022, Madau & Dickinson, 2014a, Scoville et al., 2017, Silverman et al., 2015). Constraining the size of the gas reservoirs requires probing the cool gas in these galaxies, which is not only the fuel for star formation, but also the most abundant phase in which most gas in galaxies is found (Leroy et al., 2008, Schruba et al., 2011, Walter et al., 2010). Indeed, the importance of studying molecular gas has been known, and emphasized, for decades (Dressler et al., 2009, Obreschkow et al., 2009, Walter et al., 2010), especially at higher redshifts which is essential to properly constrain the stellar density and star formation history of the Universe (Carilli & Walter, 2013).

The redshift range from $4 < z < 6$ is ideal for such work. This is the epoch immediately following the EoR but predating the so-called "modern" galaxies, i.e., galaxies at $z = 2$ at the peak of star formation density. Studying the ISM of galaxies during this epoch is critical in understanding how the galaxies which have just left their primordial roots within the EoR, evolved into modern day galaxies (Faisst et al., 2022). Not only does the molecular gas in these galaxies help study the star formation rate history over this period, it also allow for spatially resolving the ISM; we can observe the actual structure and morphology of these galaxies and learn about their kinematics and dynamics directly (Faisst et al., 2022, Walter et al., 2010). The cool molecular gas from galaxies—especially high redshift ones—can be studied using molecular and atomic fine structure lines (Walter et al., 2010).

The most common molecule in the ISM of galaxies is unsurprisingly H_2 and ideally, a study of molecular gas would involve studying H_2 directly. However, there are several factors which inhibit us from doing so: firstly, H_2 has no permanent dipole moment which makes the line difficult to detect; secondly, the ro-vibrational transitions have large ionizing potentials, which means that they require a large temperature to be excited—much higher than that of molecular clouds (Carilli & Walter, 2013, Hodge & da Cunha, 2020).

Since studying the most abundant molecule, (H_2), is not feasible, Carbon monoxide (CO), the second most abundant, becomes a natural choice (Hodge & da Cunha, 2020). CO directly traces H_2 and it has been used extensively at lower redshifts (Carilli & Walter, 2013). But unfortunately there are some drawbacks: the CO(1-0) line is faint, easily destroyed by starbursts, and it becomes more difficult to observe at higher redshifts because of dimming, lower metallicity of high-z galaxies, and higher Cosmic Microwave Background (CMB) temperature (Casey et al., 2014, da Cunha et al., 2013, Faisst et al., 2022, Hodge & da Cunha, 2020). It is also unobservable with ALMA at high redshifts since it falls outside of any of their bands. And using higher J CO emission becomes unfeasible for a large sample of galaxies (Faisst et al., 2022). It has therefore become common place to use other molecules as tracers in order to map out the cool molecular gas in galaxies. In particular, ionized and neutral carbon, nitrogen, and oxygen (Casey et al., 2014).

The far-infrared fine structure lines, from ionized gas, are strong cooling lines for the ISM (Carilli & Walter, 2013, Casey et al., 2014) and because their ionizing potentials differ from that of H_2 ([NII], and [OIII] having higher ionizing energies whilst lines like [CII], [CI], and [OI] have lower) they allow us to study various parts of the ISM including the neutral medium, H_{II} regions, and photodissociation regions (Casey et al., 2014). It is also worth noting that at high redshifts, these FIR atomic fine structure lines fall within the submm and are observable with the Atacama Large Millimeter Array (ALMA) making it one of, if not the best tool available for studying the ISM of high redshift galaxies. ALMA's incredible sensitivity and resolution have allowed us to study, only within the last decade, the ISM of "normal" main-sequence galaxies at $z > 5$. These types of galaxies are the most likely objects responsible for re-ionizing the early universe during the EoR making them invaluable objects to study (Fan et al., 2006).

There are a variety of lines from which to choose and it is therefore reasonable to ask which of them would be most appropriate.

[CII] has been used extensively to study $z > 5$ galaxies. For example, [CII] studies have been done to resolve the emitting regions around quasar hosts (Carniani et al., 2013, Casey et al., 2014, Gallerani et al., 2012, Walter et al., 2009, Wang et al., 2013), and several [CII] campaigns have been undertaken to study main-sequence galaxies (Capak et al., 2015, Faisst et al., 2022, Le Fèvre et al., 2020). [CII] has become a workhorse line for ISM studies of high-z galaxies (Carilli & Walter, 2013). There are several factors that make this one of the most ubiquitous lines in the literature: it is less affected by extinction than other SFR tracers; A survey of 10 "normal" main sequence galaxies at $z > 5$ done by Capak et al. (2015) resulted in a 100% detection rate of [CII] suggesting that the line is common amongst high-z galaxies; more than 70% of [CII] emission comes from molecular regions (Hodge & da Cunha, 2020) which makes it a good tracer of molecular gas; because it is a major cooling line (meaning that the ultraviolet radiation from newly formed stars heats up surrounding gas which is then predominately re-radiated by [CII]) it is extremely bright, often reaching 1% of the total UV luminosity (Carilli & Walter, 2013), 1000x stronger than CO(1-0). Furthermore the ALMA Large Program to Investigate [CII] at Early Times (ALPINE, Le Fèvre et al., 2020) has found [CII] to be a very good tracer of star formation (Faisst et al., 2022) which had been previously debated (Casey et al., 2014).

Recent observations of high-z galaxies have started to hint at the existence of [CII] haloes—extended [CII] emission which extend beyond the restframe UV emission. Most notably Fujimoto et al. (2019) stacked 18 main-sequence galaxies, and detected a [CII] halo signal. The results of this stacking can be seen in Figure 1.2 which shows the radial profiles of both the restframe far infrared emission, the restframe UV emission, and the [CII] emission. Other studies (e.g. Ginolfi et al., 2020a, Herrera-Camus et al., 2021, Posses et al., 2023) have begun to search for these [CII] haloes, with varying results. The existence of these haloes has only become known because of studying the cool molecular gas of main-sequence galaxies at high redshifts and may be a ubiquitous part of galaxy evolution in the early universe. These haloes allow us to study the interplay between the ISM and the Circumgalactic Medium (CGM), a reservoir of gas within a galaxy's virial radius (Tumlinson et al., 2017). All current theories on how these halo structures are made, involve feedback: satellite galaxies, photodissociation regions in the CGM, H II regions in the CGM, cold streams, outflow Fujimoto et al. (2019). Explaining how these

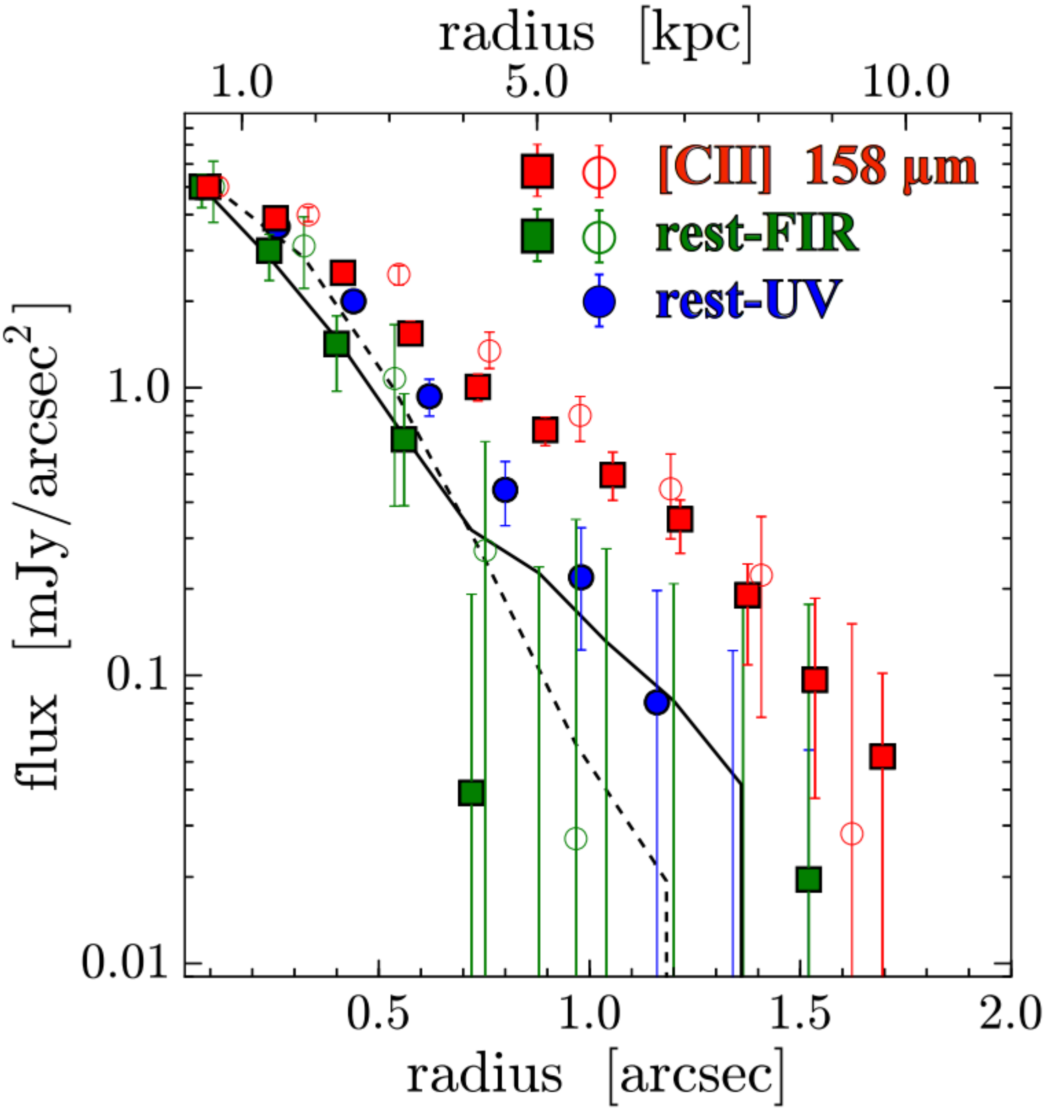

Figure 1.2: Fig. 6 from Fujimoto et al. (2019) showing the stacked [CII] profile and rest-frame UV profiles from 18 ALMA galaxies.

structures come to be is important in understanding galaxy assembly, as they might be a key evolutionary stage.

We obtained high resolution [CII] observations of a sample of main-sequence galaxies 18.1.01359.S (PI: M. Aravena). This project is in regards to combined high and low resolution [CII] observations of one galaxy in particular from that sample, namely Hz7, and what those observations revealed about its kinematics and morphological structure. The results of this study have been published in Lambert et al. (2023).

1.2 Studying galaxy evolution by studying their environments

Instead of observing the material which makes up a galaxy to study the galaxy evolution, we can also think about how their environments could have an influence. It is well known that galaxies in groups, clusters, and filaments are different from those found in voids, implying that a galaxy's environment impacts its evolution in someway (Dressler, 1980). This could be due to any number of physical mechanisms such as, but not limited to, increased merger activity, tidal gas-stripping due to the IGM, and x-ray emission within cluster environments (Gavazzi et al., 2012, Pimbblet et al., 2002, Postman & Geller, 1984).

In particular, researching environments in the early universe is essential for understanding galaxy evolution throughout cosmic time. The environments in the early universe represent the first protoclusters and filaments which collapse into the large-scale structures we see today Muldrew et al. (2015). However, identifying these structures is not easy. Normally, overdensities—groups, clusters, and other environments—are identified by mapping the galaxies which reside within them. This is possible at low redshifts, but becomes increasingly more difficult at higher redshifts as galaxies become fainter. More refined methods, or better tracers of early universe large-scale structures, are needed.

Many simulations suggest that high-z quasars near and within the EoR should be found at the cores of the largest dark-matter haloes, i.e., at the heart of early protoclusters, because many high-z quasars have supermassive black hole masses of $10^9 M_\odot$ (Bañados et al., 2013, Mazzucchelli et al., 2017a) but have had less than 1 Gyr to accrete sufficient mass and seed values are not expected to exceed $\sim 10^6 M_\odot$ in any viable scenario (Balmaverde et al., 2017, Decarli et al., 2018, Mignoli et al., 2020, Ota et al., 2018, Overzier et al., 2009). This would imply that they necessarily live in the densest environments in the early universe. If this were true then we could use high-z quasars as biased tracers of the first large-scale structures in the Universe. But whilst quasars are relatively easy to observe at high redshifts due to their incredible luminosities (quasars are the most consistently luminous objects of which we know) identifying their companion galaxies (which would indicate an overdensity) is a lot more difficult because they are much fainter. Measuring the redshifts of companions becomes spectroscopically expensive, so searches are usually conducted with photometric bands which take advantage of two distinctive spectroscopic features, namely the Lyman-Break at 912 $\mathring{A}$ and the Lyman-α (Ly-α) emission at 1216 $\mathring{A}$. Both of these features are emitted in the restframe UV, but at higher redshifts, are observable in the optical and near infrared, making them good probes of the early universe.

Photons which have wavelengths lower than 912$\AA$ have enough energy to completely ionize neutral hydrogen. Therefore any photon with a wavelength less than or equal to this limit will be completely absorbed by neutral hydrogen, either along the line-of-sight or within the galaxy itself.This lack of flux in a band bluer than 912A observed frame with respect to a band redder that it is known as the Lyman-Break. In addition, intervening HI clouds absorb Ly emission, and at z ¿ 4, this causes and intensifies the Ly-α decrement. Identifying galaxies with this abrupt change has traditionally been done using a set of broad band filters; filters centered on or bluer than the Lyman-Break will have less flux than redder filters, resulting in redder colors overall. Galaxies with a Lyman break are known as Lyman-Break Galaxies (LBGs) and this color selection technique has been very successful in identifying them at high redshifts (Dayal & Ferrara, 2018, Dunlop, 2013, Giavalisco, 2002, Stark, 2016, Zewdie et al., 2023). Figure 1.3 shows an example of how this technique works. The black line in the top panel is a spectrum, the blue, green, and red lines are filters onboard the HST. From the top panel we can see that the flux in the U band is much less than that in the other two bands. This results in the galaxy not being detected in the U-band image, as can be seen by the bottom blue panel in Figure 1.3; but it is detected in the other two bands. Photometrically, this results in a redder colors.

Alternatively astronomers can target the Ly-α line—transition from the first excited state ($n = 2$) to the ground state ($n = 1$), of any single-electron atom—most commonly hydrogen. Because hydrogen is the most abundant element in the universe, and Ly-α is emitted from the lowest energy transition level, it is one of the brightest lines available. There are also many different physical origins for Ly-α: photons which have been ionized by young stars or AGN recombining with hydrogen, collisional excitation of HI by either outlflowing or inflowing gas, or photoionization by background UV which causes hydrogen fluorescence (Ouchi et al., 2020). Young, starforming galaxies, which contain Ly-α emission, are known as Lyman-α emitters (LAEs). They are often identified via an excess of flux within a narrowband filter, centered on the expected observed wavelength for the Ly-α emission, compared to broadbands (Ouchi et al., 2020).

These two selection techniques are ideal for finding galaxies at high redshifts. Indeed, they have been used extensively to search for galaxies at $z > 5$. In particular, to search for galaxies around high-z quasars. Interestingly, the results of such studies have been varied, with some groups finding overdensities (Balmaverde et al., 2017, Decarli et al., 2019, Husband et al., 2013, Mignoli et al., 2020, Morselli et al., 2014, Utsumi et al., 2010, Zheng et al., 2006) and others not (Bañados et al., 2013, Mazzucchelli et al., 2017a, Simpson et al., 2014, Willott et al., 2005). The tension within the field is nicely summarized in Figure 1.4 which shows the results from multiple different LAE, LBG, and spectroscopic surveys over a range of field of views and redshifts.

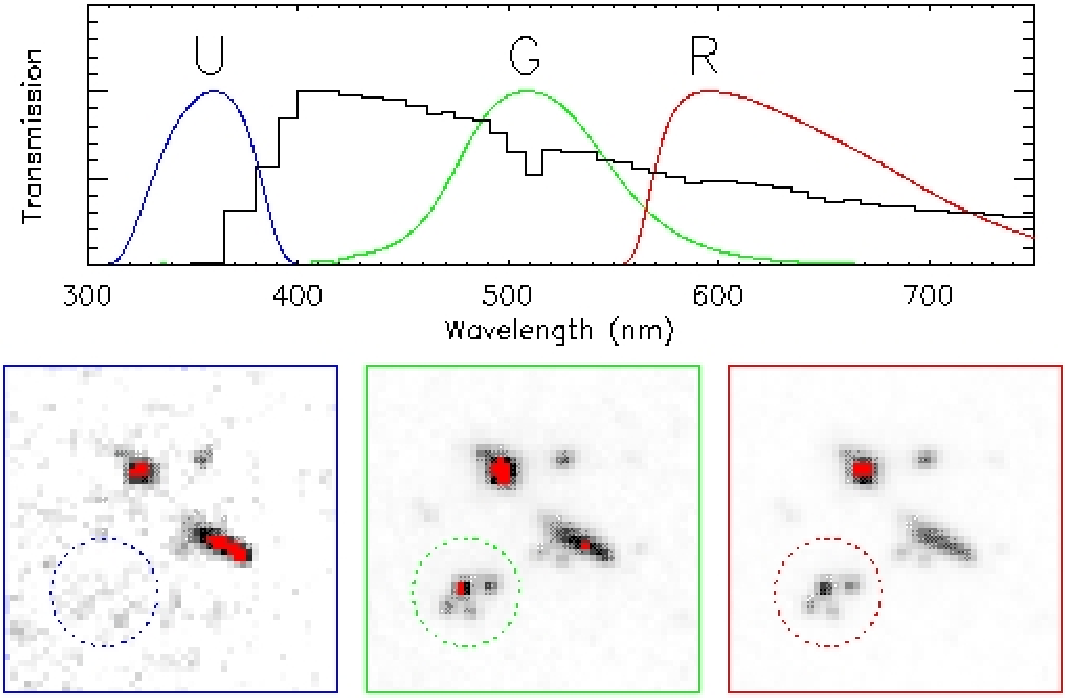

FIGURE 1.3: Demonstration behind the Lyman-Break technique for identifying galaxies. Red, Green and Blue lines represent the R, G, and U filters on the Hubble Space Telescope. The black histogram in the top panel is a Lyman-Break spectrum. The bottom panel shows the images in each of the corresponding filters. Dashed circles in each of the images shows the location of the galaxy. Graphic taken from Niels Bohr Institute and is available at `https://www.nbi.dk/~jfynbo/LBG.html`

The wide variety of results across methods, redshifts, field of views, and targets means the question: “do quasars live in over dense environments?” remains unanswered. And only by addressing certain observational effects, which might have influenced previous studies, will we be able to answer the question.

Using the Dark Energy CAMera (DECam), housed on the 4m Blanco telescope at the Cerro Tololo Inter-American Observatory (CTIO), we observed a high-redshift quasar, with a confirmed ALMA [CII] redshift of $z = 6.9018 \pm 0.0007$ (Venemans et al., 2015), in i, z, and narrow bands, in order to identify LAEs. This telescope has a ~ 3 square degree field of view, making this search the largest FoV search of this kind ever done (see the red star in Figure 12). By using a [CII] redshift and an enormous field of view, we take into account the observational biases which might have affected previous LBG and LAE searches and answer the question of whether quasars truly live in overdense environments in the early universe.

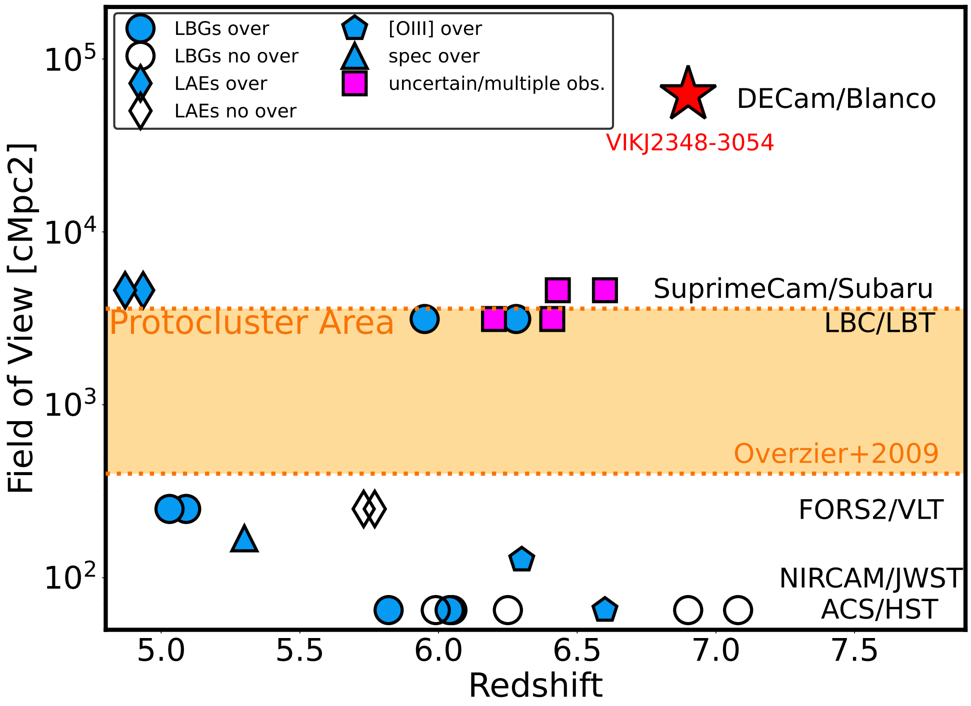

FIGURE 1.4: Field of view vs the redshift of multiple overdensity searches around high-z quasars. The red star indicates where these observations lie with respect to the literature. The yellow area is the theoretical size of a protocluster at $z = 6$ from Overzier et al. (2009).

1.3 The layout of this thesis

This thesis consists of four chapters: this introduction, [CII] observations of Hz7 with ALMA, exploring the the environment around VIK J2348–3054, and finally conclusions and future work. Chapter 2 has already been published (Lambert et al., 2023), and Chapter 3 is to be submitted within a couple of weeks (Lambert et. al., in prep). As such, I have left them in their original formats and note that this does introduce slightly awkward wording. For example the use of “in this paper” when it is presented in a thesis. Furthermore, the observant reader will notice a change of pronouns throughout the thesis; in Chapters 2 and 3, I make extensive use of the pronoun “we” to refer to myself and the numerous collaborators on these two individual projects. Considering the enormous amount of help I received from them, as well as the collaborative nature of science as a whole, it is only right to leave this unchanged even though this thesis is my own work.

Chapter 2

An extended CII halo around a massive star-forming galaxy at $z = 5.3$

2.1 Introduction

Studying the kinematics and structures of galaxies at high redshifts is fundamental in developing a full understanding of mass assembly, galaxy evolution, and exploring the epoch of reionization. However, galaxies in the high-redshift regime ($z > 4$) have faint ultraviolet (UV)/optical apparent magnitudes due to cosmic dimming which can significantly increase the difficulty of probing meaningful samples with increasing redshift (Bradley et al., 2008, Ellis et al., 2001, Linzer & Steinhardt, 2020, Steinhardt et al., 2021, Zheng et al., 2012). The objects that are identified and studied at these redshifts are often either luminous quasars, massive starbursting galaxies, or both (e.g. Ellis et al., 2001). To obtain a detailed view of the properties of galaxies in the early universe, it is important to obtain and analyze observations of "normal" galaxies, i.e. L^* or near L^*. These galaxies tend to dominate the star-formation density of the universe across all redshifts including at the epoch of reionization ($z > 6$; Madau & Dickinson, 2014b). Probing the physical conditions of these galaxies has only been made possible due to large technological improvements over the past two decades with facilities such as the Atacama Large Millimeter/submillimeter Array (ALMA), The Hubble Space Telescope (HST) after the addition of the Wide Field Camera 3 (WFC3), and recently, the James Webb Space Telescope (JWST).

HST deep field integrations have identified and quantified galaxies' contribution to the cosmic star formation rate (SFR) density out to $z \sim 10$ (Bouwens et al., 2022a,b, Ellis et al., 2013, Livermore et al., 2017, Oesch et al., 2018, 2016, Stefanon et al., 2021, 2022). However, the physical mechanisms for growth in these galaxies remain unknown. Studying the morphology, and subsequently, the kinematics of these galaxies proves difficult since UV continuum and Lyman α emission are significantly absorbed by dust and by neutral hydrogen in the intergalactic medium (IGM) respectively (Carniani et al., 2017, Maiolino et al., 2015, Massa et al., 2022). Therefore, different tracers of star-formation and the properties of the inter-stellar Medium (ISM) gas are required.

ALMA has allowed for high angular resolution observations of high-redshift galaxies (e.g. Carniani et al., 2017). This is typically done by observing the [CII] 158 μm line, which is one of the brightest emission lines we can observe (reaching up to 1% of the total bolometric luminosity; Díaz-Santos et al., 2013, 2017). The [CII] emission is a remarkable tracer of the ISM as it is the main line for cooling neutral gas in normal star-forming galaxies (Bouwens et al., 2022b, Capak et al., 2015, Matthee et al., 2019, Schaerer et al., 2020); moreover, it is not affected by obscuration as much as UV and Lyman α emission. This makes [CII] an ideal line to probe the morphologies and kinematics of distant sources, particularly at z¿4, where it shifts into more transparent (sub)millimeter atmospheric windows.

A pilot ALMA [CII] survey - carried out using an early version of the array- observed ten galaxies at z $\sim$ 5 (Capak et al., 2015). Nine of them were chosen as Lyman-break galaxies (LBGs) in the Cosmic Evolution Survey (COSMOS) field (Scoville et al., 2007) with spectroscopic confirmation of their redshifts from the Deep Extragalactic Imaging and Multi-Object Spectrograph (DEIMOS) on the W.M. Keck-II Telescope in Hawaii (for more information on the selection criteria see Capak et al. (2015). Comparisons between these observations and rest-frame ultra-violet (UV) observations—taken using the Advanced Camera for Surveys (ACS) on HST—show the infrared excess (IRX $\equiv L_{\rm IR}/L_{\rm UV}$) ratio at a given UV-slope β to be substantially lower than expected according to current models, as can be seen in Figure 2 of Capak et al. (2015). This result was later confirmed by Barisic et al. (2017). This suggests that there is substantial evolution taking place very early on in the universe, at the epoch of reionization, since current models cannot account for the excess in [CII] emission of these sources.

To determine what evolutionary processes might be occurring within galaxies during this epoch, we have taken high angular resolution observations of some of these galaxies to explore their morphological and kinematic properties. In this chapter we study the observations of HZ7 in particular, one of the brightest objects in the Capak et al. (2015) sample, with a rest-frame UV spectroscopic redshift of z = 5.2532±0.0004 (Capak et al., 2015). This galaxy seems to be a "normal" galaxy based on its location with respect to the main sequence of star forming galaxies (near L^*), at those redshifts (Capak et al., 2015, Speagle et al., 2014). Furthermore, it has good multiwavelength coverage (Capak et al., 2015, Leauthaud et al., 2007, Posses et al., 2023), which makes it an excellent target.

Of particular interest is the idea of "[CII] haloes", which have been suggested in order to explain the observed distribution of gas and the star-formation in high-redshift galaxies (Fujimoto et al., 2019, 2020, Ginolfi et al., 2020a). Previous studies have identified extended [CII] emission, or [CII] haloes, using low-resolution ALMA imaging ($\sim$ 1.0" beam; Fujimoto et al., 2020, Ginolfi et al., 2020b). So far, only two similar main sequence ("normal") galaxies have been studied with high-resolution [CII] imaging (0.3"), in this redshift range, enabling a clear determination of the existence of a [CII] halo: Herrera-Camus et al. (2021) found a [CII] halo whilst Posses et al. (2023) did not. There are several suggested physical mechanisms that might lead to such haloes including the presence of satellite galaxies, circumgalactic H_{II} regions, cold streams of gas, outflows, mergers, and photodissociation (these physical mechanisms are discussed in more detail below).

We note that this is an unusual use of the term "halo", as it is often used to describe particular astrophysical components of a galaxy, for example: dark matter haloes, stellar haloes, and galactic haloes—which are usually spheroidal in shape. However, the widespread use of the term in the recent literature has provided a strong precedent for [CII] haloes to refer to extended, fuzzy [CII] emission around high-redshift galaxies (Fujimoto et al., 2019, 2020, Ginolfi et al., 2020a, Herrera-Camus et al., 2021, Pizzati et al., 2020, Posses et al., 2023). In order to remain consistent with the current literature on the topic, we will make use of the term "[CII] halo" but we emphasize that we strictly refer to extended [CII].

Here we present high signal-to-noise ALMA [CII] follow-up observations of HZ7 at an angular resolution comparable to that of HST and JWST. The new observations allow us to probe of the [CII] and the rest-frame UV emission at similar scales, and search for potential extended [CII] emission.We discuss previous as well as our own observations of HZ7 in §2. The analysis and results are described in §3, followed by a discussion in §4. Our summary and conclusions are found in §5. Throughout this chapter we adopt a vanilla ΛCDM cosmology with $\Omega_m = 0.3$, $\Omega_\Lambda = 0.7$, and $H_0 = 70$ km s^{-1} Mpc^{-1}.

2.2 Data

2.2.1 Target Selection and Physical Properties

HZ7 is part of the sample of galaxies presented by Capak et al. (2015). These objects were selected as LBG candidates within the COSMOS field, with spectroscopically determined redshifts. They all have luminosities between 1 and 4 L^* and with β between -1.4 and -0.7 (Capak et al., 2015).

HZ7 was detected at a redshift of z = 5.25 and was detected by Capak et al. (2015) in [CII] with a peak flux density of $\sim$ 2 mJy. An upper limit of 36 μJy was determined from the 158μm continuum emission, implying that there may be low dust content or that HZ7 is an outlier in the IRX-β relation. Capak et al. (2015) also estimated a SFR of 21^{+5}_{-2} $M_{\odot}yr^{-1}$ using the Kennicutt (1998) relation (Capak et al., 2015, Ota et al., 2014) and a combination of UV and far-infrared data, as well as an upper limit of 10.35 $L_{\odot}$ for the IR luminosity. The IR Luminosity was determined by fitting grey body models, available in Casey (2012). Capak et al. (2015) estimated a stellar mass of 9.86 ±0.21 $M_{\odot}$ and a dynamical mass of $10.8^{+1.5}_{-1.0}$ $M_{\odot}$ by fitting Bruzual and Charlot templates (Bruzual & Charlot, 2003) to COSMOS photometry as done previously in Ilbert et al. (2013) and using the method in **?** to derive the dynamical mass from the [CII] velocity dispersion.

2.2.2 ALMA Observations

The target HZ7 was observed as part of the ALMA project 2018.1.01359.S (PI: M. Aravena). At the redshift for HZ7 of z = 5.2532±0.0004 (Capak et al., 2015) the [CII] line is centered at 303.9292 GHz which falls into the ALMA band 7 (275 GHz – 373 GHz). The observations were carried out on 2018-11-28 with a total of 80 minutes of on-source integration time.

During the observation, two overlapping spectral windows (SPWs) were placed to detect the [CII] emission and two were placed in the opposite side-band to map the continuum at a rest-frame wavelength of 161.5μm. The ALMA observatory staff, as part of standard pipeline, performed initial data calibration. The calibrated visibility data were then re-analyzed, performing additional flagging of bad time periods in the data and bad channels. We concatenated the new ALMA observations with that obtained by Capak et al. (2015). The previous data was taken in a more compact configuration providing extra sensitivity to extended emission. The data were re-imaged using a natural weighting of the u-v visibility data to create continuum, moment zero, and channel maps with an average beam size of 0.27”. Gaussian fitting of the spectral and spatial data was performed using the Common Astronomy Software Applications (CASA) software viewer and associated fit tools (McMullin et al., 2007). The continuum and line images were interactively cleaned by manually masking out the emission.

Since the residual map which results from the CLEAN algorithm can have incorrect default flux scaling when combining different array configurations (Jorsater & van Moorsel, 1995), we apply a correction as suggested by Czekala et al. (2021). This correction makes an important difference with regards to the total flux density measurements of HZ7 (resulting in a 33% decrease in the peak flux density), but very little, to no qualitative difference with respect to the spatial distribution. We remark that the main results presented in this chapter remain the same when using only the new ALMA data and no artificial structures are added when combining with data from Capak et al. (2015).

2.2.3 HST Observations

HST/WFC3 observations of HZ7 in the F105W (10430.83 Å), F125W (12363.55 Å), and F160W (15278.47 Å) bands were obtained from the Hubble Legacy Archive (PID:13601), and are used in this work to compare the rest-frame UV emission as traced by these images with the [CII] emission observed by ALMA. These data products were corrected astrometrically by calibrating them to the GAIA DR2 release (Gaia Collaboration et al., 2018a). We queried the DR2 release using the python package `astroquery.gaia` [1]. Using the positional information within the HST headers and then manually associated each GAIA star with a star in the HST image. The difference in position between the DR2 release and the actual stars in the HST images renders the offset which is then applied to the HST images. The average offset was $\sim 0.300 \pm 0.008$” ($\Delta\alpha = -0.128$”; $\Delta\delta = 0.283$”) [2].

2.3 Analysis and Results

2.3.1 Spatially integrated emission line

Figure 2.1 shows the spatially integrated spectrum of HZ7. This plot was created following the procedure in Béthermin et al. (2020), which was also used in Endsley et al. (2022) and Schouws et al. (2022). This is an iterative process where a small aperture equal to the area of the beam width is centred on the main source of emission ($\alpha =$

---

[1] `https://astroquery.readthedocs.io/en/latest/gaia/gaia.html`

[2] Full GAIA calibration and routine is available at `https://github.com/TrystanScottLambert/Hz7_ISM/blob/main/Align.py`

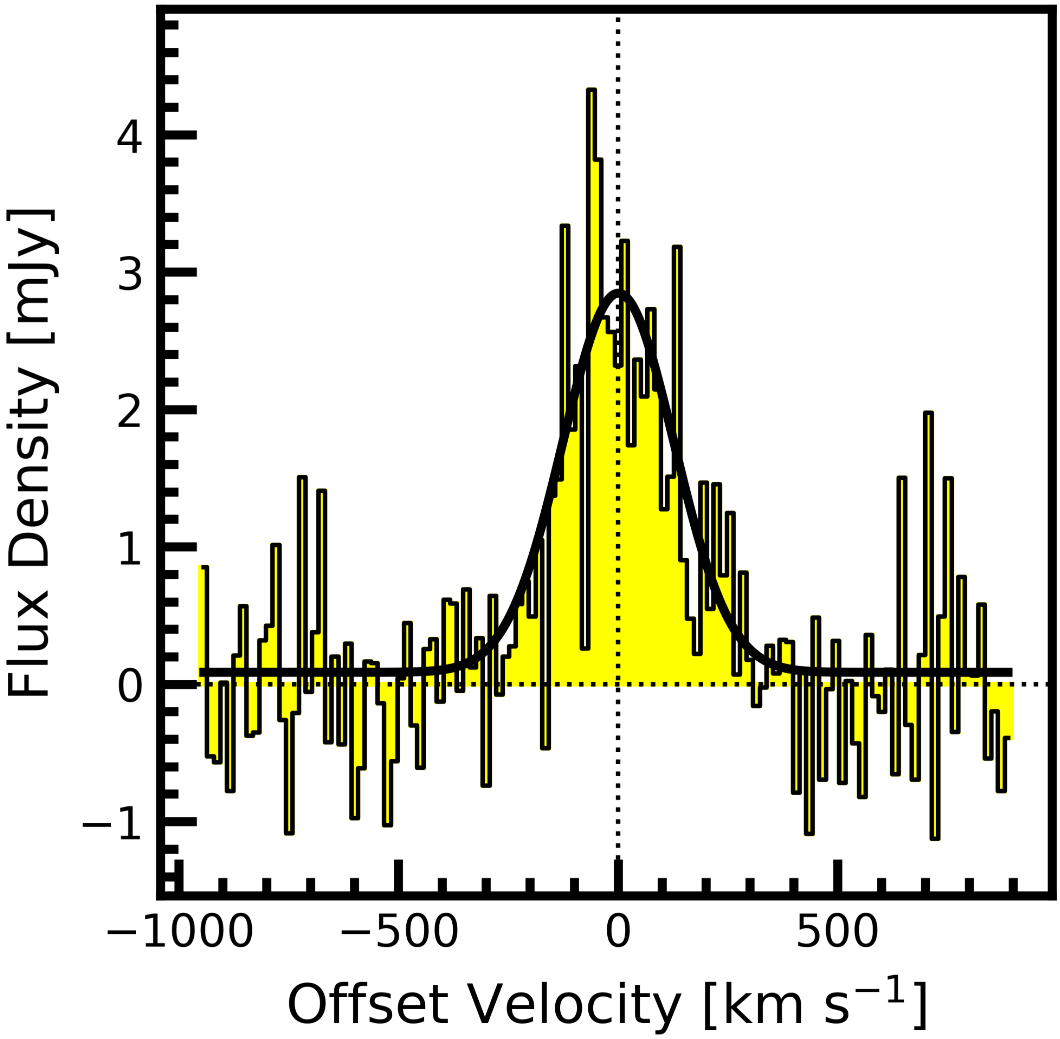

FIGURE 2.1: Spatially integrated spectrum of [CII] emission toward HZ7 at z = 5.25, at a channel (spectral) resolution of 15 km s^{-1}, using a combination of the new high resolution data and those reported in Capak et al. (2015).

09:59:30.459, δ = 2.08.02.586); using this aperture, an integrated spectrum is extracted and a Gaussian profile can be fitted to the emission; the full width at half maximum (FWHM) from this fit is used to create a simple moment-0 map which in turn provides a mask—by taking all emission greater than 3σ—and then masks the entire cube. This masked cube is used to extract another integrated spectrum, and the process is repeated, until the extracted integrated spectrum remains unchanged. The shape and integrated flux of the spectrum is similar with that obtained by Capak et al. (2015) with a FWHM of 298 ± 27 km s^{-1} and an integrated flux density ($S_{\rm [CII]}$) of 0.86 ± 0.11 Jy km s^{-1} (as compared to 380 ± 42 km s^{-1} and 0.71 ± 0.07 Jy km s^{-1}). We calculate the [CII] line luminosity to be $\log\left(L_{\rm [CII]}/L_\odot\right) = 8.8 \pm 0.1$—very close to the value of 8.74, estimated by Capak et al. (2015).

Table 2.1: Measured and derived properties as well as literature values of Hz7.

Property	Value	Reference
$z_{\text{[CII]}}$	5.2532 ± 0.0004	Capak et al. (2011)
$S_{\text{[CII]}}$	0.86 ± 0.11 Jy km s^{-1}	this work
$\log(L_{\text{[CII]}}/L_{\odot})$	8.8 ± 0.1	this work
[CII] FWHM	298 ± 27 km s^{-1}	this work
$\sigma_{\text{[CII]}}$	127 ± 12 km s^{-1}	this work
RA	149.876986°	Capak et al. (2015)
Dec	2.134113°	Capak et al. (2015)
SFR	21^{+5}_{-2} M$_{\odot}$ yr^{-1}	Capak et al. (2015)
$Y_{105\text{W}}$	24.56 ± 0.04	Barisic et al. (2017)
$J_{125\text{W}}$	24.37 ± 0.04	Barisic et al. (2017)
$H_{160\text{W}}$	24.28 ± 0.04	Barisic et al. (2017)
$\log(M_{\odot})$	9.86 ± 0.21	Capak et al. (2015)

2.3.2 Spatial and velocity distribution of [CII]

The frequency integrated [CII] emission, velocity field, and dispersion map are shown in Figure 2.2. The channels which were collapsed to create these maps, were selected by using the Gaussian fit in Figure 2.1. Specifically, we chose all channels within the FWHM, which resulted in 18 channels on either side of the central emission channel—a velocity range of 540 km s^{-1}.

The higher-order moment maps provide essential information but can often be difficult to interpret without masking; i.e. focusing only on the area of the map which contains the emission and ignoring the rest. We used the integrated [CII] emission to build masks for the velocity field and dispersion map, by taking all emission greater than 3σ within the moment-0 map. The integrated emission of HZ7 shows a galaxy with a centrally bright concentration of light. However, the emission is elongated in the NE direction with significant structure. This can be seen by the tendril-like appendage to the north east as well as the small knots of emission around the center of the galaxy.

Contrary to the integrated [CII] emission, the velocity field and dispersion map do not show ordered structures. Both higher-order moment maps are disordered with the velocity field in the middle panel of Figure 2.2 showing no indication of a gradient and therefore no clear indication of a rotating disk. Likewise, the velocity dispersion map in the bottom panel of Figure 2.2 shows significant structure which is in stark contrast to the well-behaved brightness distribution of the integrated [CII] emission. The disturbed morphology, and the likely turbulent ISM—inferred from the large emission line width—suggests that HZ7 could possibly be a merging system and not a single galaxy.

Both the integrated spectrum (Fig. 2.1) and the integrated [CII] emission (top panel of Fig. 2.2) are used to derive several source properties of HZ7 in the following sections.

The source information can be found in in Table 2.1, along with previous measurements for this source in the literature.

2.3.3 Spatial distribution of [CII], rest-frame UV, and dust continuum

We present the spatial distribution of the dust continuum emission in Figure 2.3 with blue contours. The continuum dust emission, unlike the [CII] emission, is not smooth and is instead clumpy with a central source overlapping the central emission in both [CII] (contoured in red), and the rest-frame UV (represented by the background in gray-scale). Figure 2.3 shows that the spatial distribution of the [CII] emission is extended beyond that of the rest-frame UV as well as the continuum. The dust continuum emission appears to be more extended than the rest-frame UV and contains a southern extension which surpasses even the [CII] emission. More detailed discussion on the physical interpretation of Figure 2.3 follows in §4.

2.3.4 [CII] compared to rest-frame UV

A radial profile was generated by placing a series of increasingly larger annuli, in bins of 0.1", around the peak [CII] emission of the moment-0 map. This peak was determined by summing up the emission along the RA and Dec axis independently and then determining the central RA and Dec values which were calculated from the resulting two, independent, 1-D Gaussian fits. The total flux in each annulus was then calculated and normalized by the area represented by each respective annulus. The uncertainty of each annulus was calculated as

$$u\left(F\right) = \sqrt{n\sigma^2 + F}, \tag{2.1}$$

for the HST images and

$$u\left(F\right) = \sigma\sqrt{\frac{n}{n_{\mathrm{beam}}}}, \tag{2.2}$$

for the [CII] moment-0 map, where σ is the RMS, F is the total flux within the annulus, n is the number of pixels within an annulus, and n_{beam} is the number of pixels in a beam area. The results of constructing this radial profile can be seen in Figure 2.4. A Sérsic profile was adopted in order to fit the radial profiles using a Monte-Carlo Markov-chain fitting routine, with the python package `emcee` Foreman-Mackey et al. (2013).

To appropriately compare morphologies between the HST and ALMA data, the high resolution HST data was convolved with the ALMA beam. The Sérsic free-index radial profiles of all the available HST data—F105W, F160W, and F125W—are compared to the free index Sérsic fit of the [CII] emission and is shown in Figure 2.4. The centers

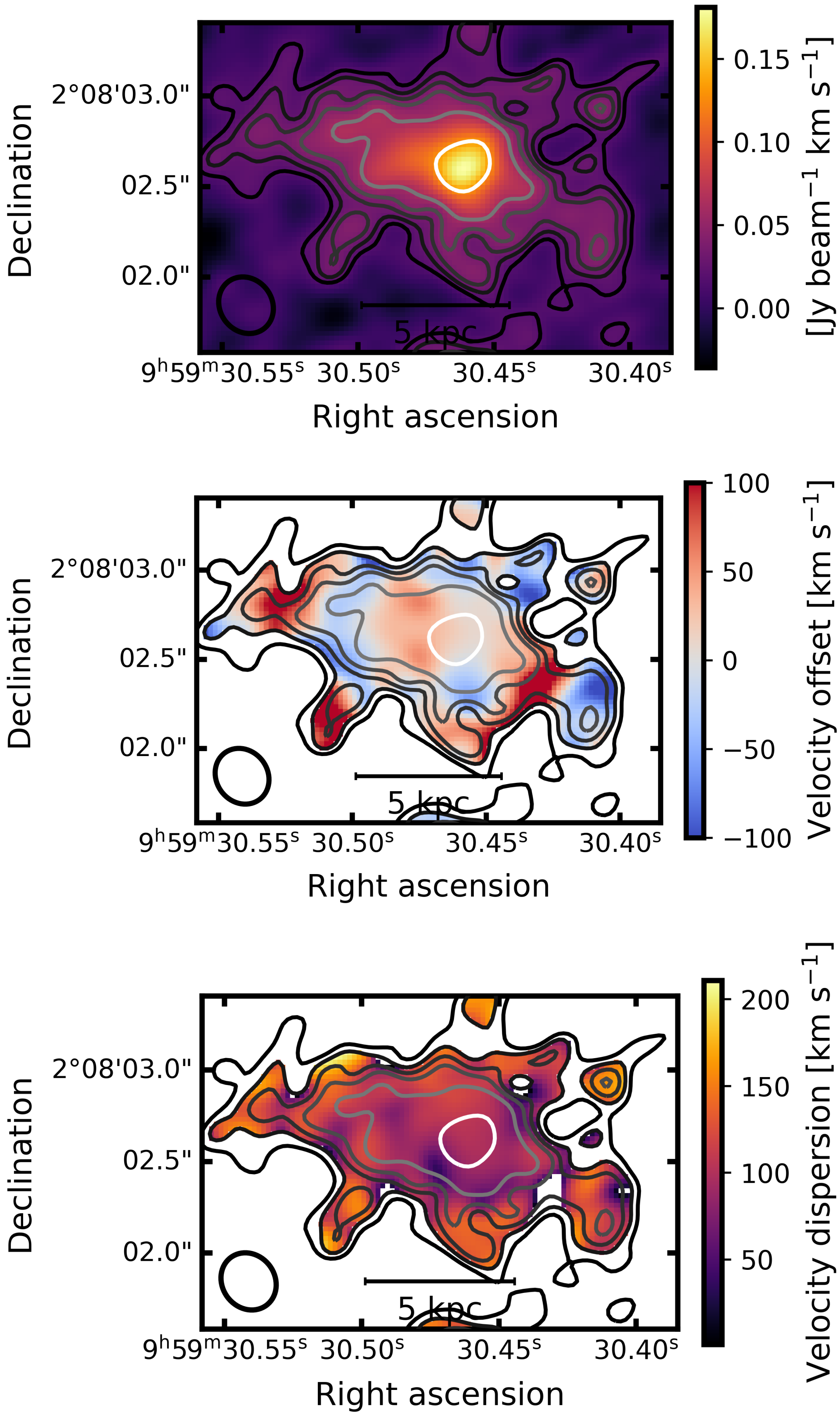

FIGURE 2.2: TOP: Integrated [CII] emission the HZ7 galaxy with $\sigma = 0.02$ Jy beam^{-1} km s^{-1}. Contours show the 2, 3, 4, 5, 7, and 15 σ levels of the rms of the integrated emission. These contours are overlaid in the moment-1 and moment-2 maps below. MIDDLE: [CII] Velocity Field of the HZ7 galaxy. BOTTOM: Dispersion map of the [CII] detection of the HZ7 galaxy.

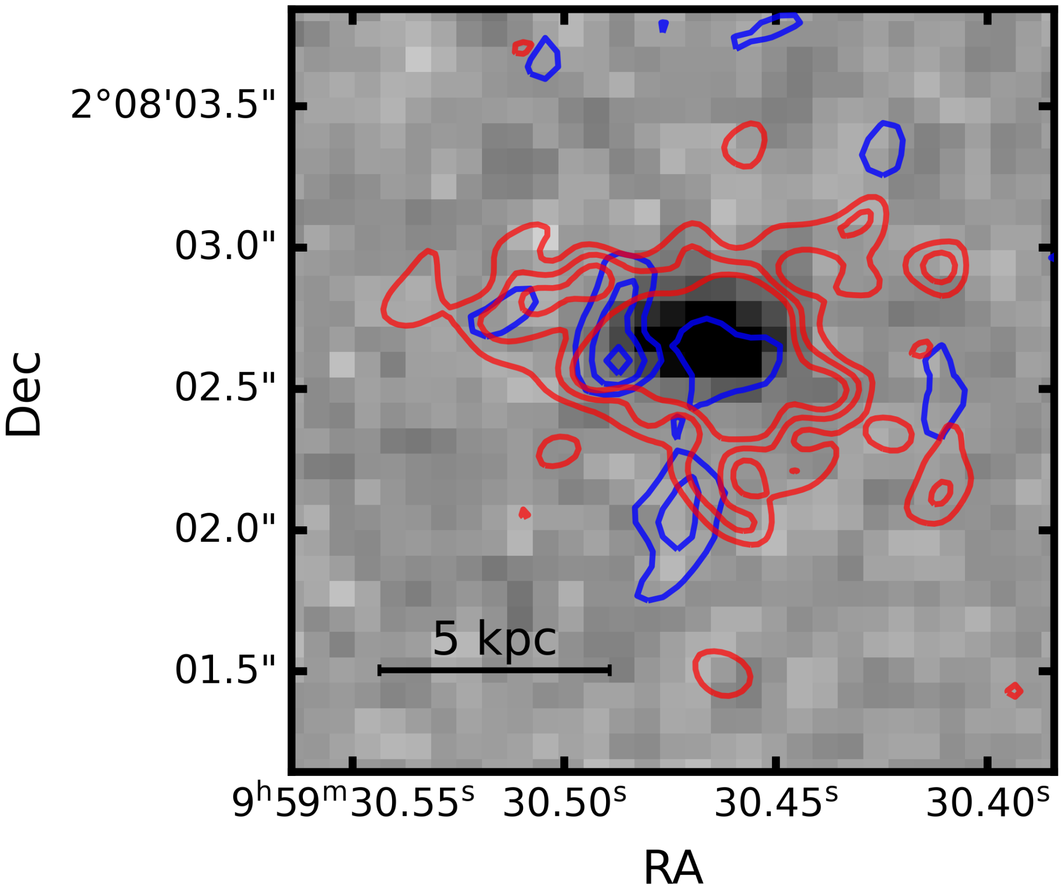

FIGURE 2.3: Comparison of the rest-frame UV, [CII] and dust continuum emission toward HZ7. The gray-scale background represents the Y band HST observation. Red contours (3-5 σ) represent the integrated emission from the ALMA [CII] data whilst the blue shaded contours (2-5 σ) are that of the continuum emission.

of the individual HST filter images were determined in the same manner as the [CII] profile (explained earlier); therefore, any residual systematic offset between the [CII] and rest-frame UV emission do not affect the final results. The best-fit effective radii and Sérsic indices are given in Table 2.2. The comparison between the [CII] and rest-frame UV radial profiles show that the effective radius of the [CII] emission is 2 - 3 times larger than that of the UV emission. The two dashed lines show the R_e parameter of the Sérsic fit of the [CII] emission and the average R_e parameter for all the HST filters. To compare all the fitted profiles in the same scale, and to be comparable to what is usually adopted in the literature, we also used a fixed Sérsic index of 1.0. In this case, the obtained [CII] sizes are still 2x larger than those of the rest-UV.

In addition to the UV and [CII] radial profiles, we also compare their surface distributions in Figure 2.3. Although more affected by S/N, the surface distribution analysis allows the added benefit of spatial information which itself can be important to the understanding of the underlying physical processes. We once again see that the the [CII] emission is far

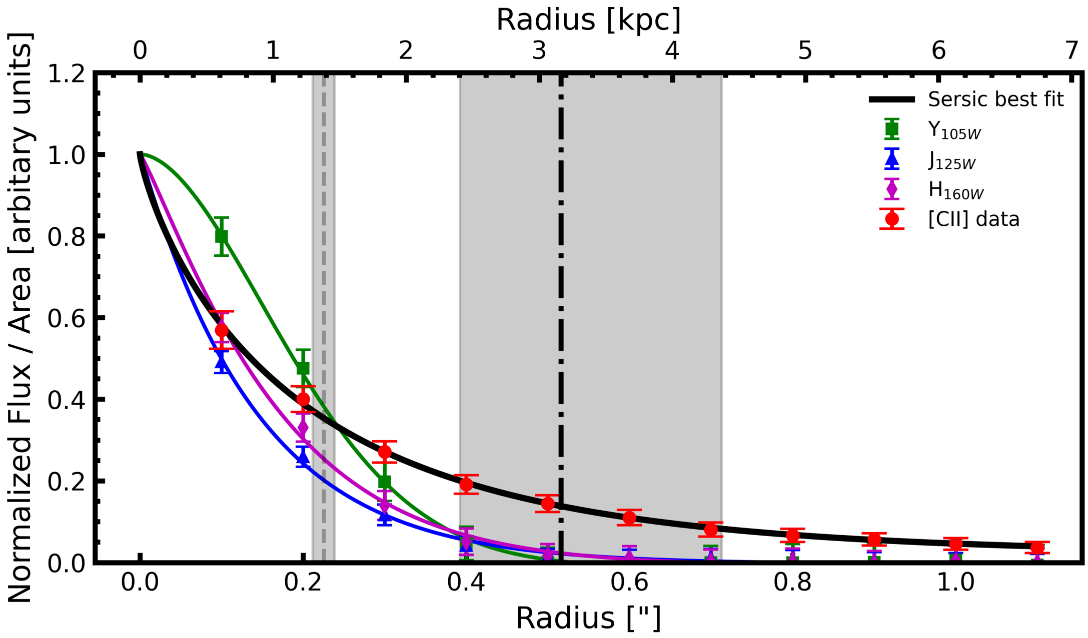

FIGURE 2.4: Fitted Sérsic profiles of the [CII] with a Sérsic index of 0.9 (black line) as well as the UV emission from HST in the F105W, F125W, F160W and total UV emission (shown as green, blue, and magenta lines respectively). The vertical dashed and dot-dashed lines highlight the average effective radius from the UV Sérsic fits and the effective radius from the [CII] Sérsic fits respectively.

more extended than that of the rest-frame UV emission. This is qualitative confirmation of this extension found for the radial profiles.

2.4 Discussion

Recent studies of massive star forming galaxies at z=4-6 have found the almost ubiquitous presence of [CII] line emission extending beyond the location of star forming regions traced by the rest-frame UV (Fujimoto et al., 2019, 2020). Such [CII] observations have been mostly conducted at low angular resolution (1.0") or through stacking analysis, hindering the physical mechanisms that might produce such haloes or making it unclear whether the extended [CII] emission is partly due to the nature of the observations. HZ7 is amongst the first galaxies at these redshifts ($z > 4$) with clear evidence for a smooth and wide [CII] emission, along with HZ4 (Herrera-Camus et al., 2021).

2.4.1 Morphology and Kinematics

HZ7 has a series of clumpy [CII] regions. The integrated emission shown in Figure 2.2 shows knotted regions of significant [CII] concentration, in addition to the main central

TABLE 2.2: Best-fit parameters for the Sérsic fits of the HST filters as well as the [CII] emission.

Wavelength	R_e ["]	R_e [kpc]	Sérsic Index
[CII]	$0.59^{+0.08}_{-0.10}$	$3.60^{+0.49}_{-0.64}$	$1.28^{+0.21}_{-0.27}$
Y_{105W}	$0.20^{+0.02}_{-0.03}$	$1.23^{+0.11}_{-0.16}$	$0.55^{+0.13}_{-0.22}$
J_{125W}	$0.24^{+0.04}_{-0.11}$	$1.47^{+0.24}_{-0.69}$	$1.04^{+0.37}_{-0.87}$
H_{160W}	$0.23^{+0.04}_{-0.10}$	$1.41^{+0.21}_{-0.58}$	$0.83^{+0.29}_{-0.74}$
[CII]	$0.50^{+0.04}_{-0.04}$	$3.07^{+0.23}_{-0.25}$	1
Y_{105W}	$0.24^{+0.02}_{-0.03}$	$1.48^{+0.15}_{-0.16}$	1
J_{125W}	$0.24^{+0.02}_{-0.03}$	$1.44^{+0.14}_{-0.15}$	1
H_{160W}	$0.23^{+0.03}_{-0.03}$	$1.51^{+0.17}_{-0.18}$	1

[CII] emission. There are potentially several physical reasons that could explain these isolated peaks. However, no counterparts to these structures can be found in the rest-UV emission map shown in Figure 2.3. Figure 2.2 shows that the main, central [CII] emission has a "smooth" distribution. The central [CII] emission and the central UV emission are well aligned but the dust continuum is less present within this central region and has a reasonably large southern extension without any UV emission.

The velocity map (middle panel of Fig. 2.2) does not have any gradient and does not show any preferred state of motion. The possible explanations are varied and might include dynamical disturbance. This would be evidence of a possible merger (Le Fèvre et al., 2020, Romano et al., 2021). This is further backed by the dispersion map (bottom panel of Fig. 2.2) which, once again, does not show any kind of preferred, or ordered motion. Both the moment-1 and moment-2 maps show that this is a complex kinematical system.

2.4.2 [CII] Halo

In §3.4 we presented evidence of a large [CII] emission which is roughly double or triple that of the UV emission. A possible interpretation of such a result is the existence of a [CII] halo (Fujimoto et al., 2019, Ginolfi et al., 2020a, Pizzati et al., 2020). What makes the case of HZ7 interesting is that unlike Fujimoto et al. (2019) and Ginolfi et al. (2020a), our results are not derived through stacking of a large sample of galaxies, but are rather inferred from direct measurements of the halo extension in a single target. Fujimoto et al. (2019) stacked a sample of 18 normal galaxies (including HZ7) in the redshift range $5.153 \leq z \leq 7.142$. Both Fujimoto et al. (2019) and this work's UV results fall well within the average values expected for normal star-forming galaxies at these redshifts as calculated by Shibuya et al. (2015). Notably, we found the ratio of the [CII] effective radius to the rest-frame UV effective radius ($R_{\mathrm{eff,[CII]}}/R_{\mathrm{eff,UV}}$) to be ~ 3 which strongly agrees with the result from Fujimoto et al. (2020, see their Fig. 3) and exceeds the ratio found by Herrera-Camus et al. (2021) of 1.2, who detected a [CII] halo within HZ4, which occupies a similar position to HZ7 on the main sequence.

Fujimoto et al. (2020) provides a test to determine if a system has a [CII] halo: masking out a beam-sized area of central [CII] emission, and all emission greater than 10 kpc, which results in an annulus of [CII]; if the remaining emission is greater than 4σ, then the system can be considered to have a [CII] halo. HZ7 meets this requirement. However, as has been stated by Herrera-Camus et al. (2021), this test is purely observational in nature; it is only dependent on the galaxy size vs the beam area and does not take into account any other information besides the [CII] observation, ignoring rest-frame UV data. Therefore, Herrera-Camus et al. (2021) suggest a more physical, but similar, definition: measuring if the extended [CII] emission—the emission which extends further than the rest-frame UV emission—is greater than 4σ. In both definitions, HZ7 is considered a system with a [CII] halo.

2.4.2.1 Physical Interpretations

Fujimoto et al. (2019) lists 5 physical possibilities for [CII] haloes in high-redshift galaxies: (i) the existence of satellite galaxies, (ii) circumgalactic photodissociation regions, (iii) circumgalactic H_{II} regions, (vi) cold streams, and (v) outflows. In the case of HZ7, it is not possible to determine the exact physical process or processes behind the observed [CII] halo from these ALMA observations alone. Fujimoto et al. (2019) could only go so far as to exclude satellite galaxies as the physical reason due to a lack of stellar continuum emission within the haloes but could not definitively differentiate amongst the other four. Later, Pizzati et al. (2020) proposed a physical model to explain these [CII] haloes—suggesting that supernovae-driven cooling outflows are the most likely reason (see Ginolfi et al., 2020a).

We checked for extended velocity components across the galaxy, which would imply the presence of an outflow, following the analysis of Herrera-Camus et al. (2021). This involved placing seven small apertures (once with radii of 0.05" and once with 0.02") around the source (Fig. 2.5). The [CII] profiles of each of these apertures were then examined. However, we found that there was no evidence for an outflow, which would be identified as an offset or wider secondary line components in the spectra, at the sensitivity

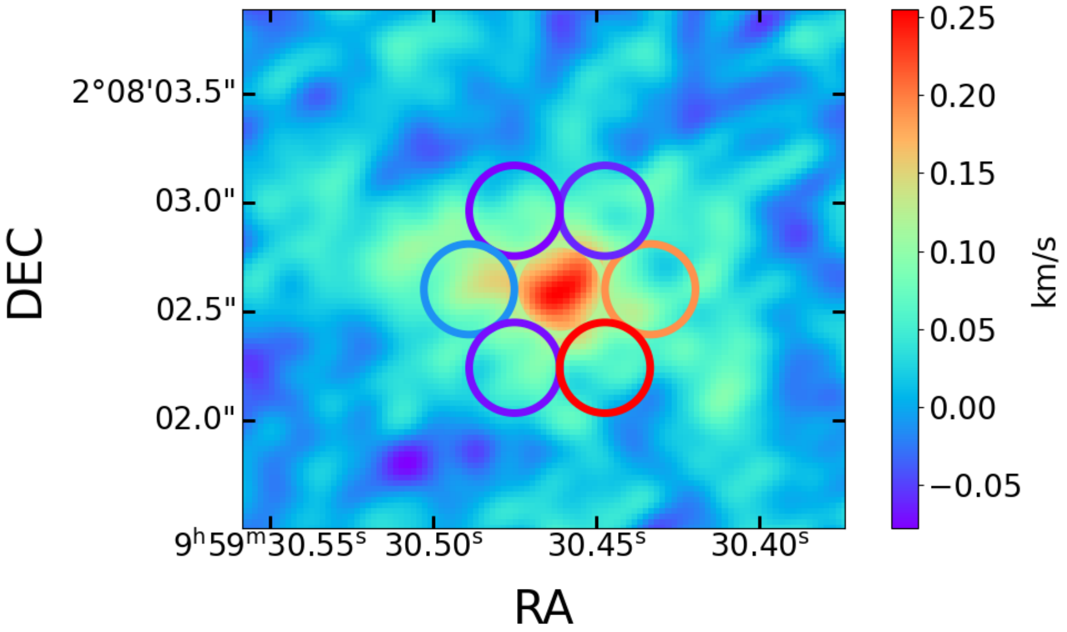

FIGURE 2.5: Circular Analysis results as per Herrera-Camus et al. (2017). Each circle represents an aperture that was used to extract a spectrum along the velocity axis. These spectra were fitted with Gaussian-fits. The resulting central velocity was used to color each respective circle.

of our observations. Herrera-Camus et al. (2021) managed to measure these offsets in HZ4 thus suggesting outflows as the physical process associated with the creation of that halo. This could imply that either deeper, or higher signal-to-noise, observations might be necessary in order to detect evidence of outflows.

Hints about the origin of this halo can be taken from the continuum emission shown in Figure 2.3. Both the dust continuum and the [CII] have some emission overlapping the peak of the UV emission. The eastern emission in continuum overlaps with the eastern extension of [CII], but is lacking in UV emission. Detectable dust emission in this area combined with a discernible lack of UV emission suggests that the latter is being suppressed due to dust obscuration. This could possibly explain the existence of [CII] haloes in the first place, implying that what we observe as [CII] haloes are in fact due to dust obscuration suppressing the total UV emission. But based on these results of HZ7, the galaxy would be dust poor towards the center, which seems unlikely. There would also be an expectation for the [CII] and dust emission to be aligned, and dust emission towards the outskirts of the system. Both of these criteria are not observed in this data. In particular, current theory suggests that galaxies tend to have dust centrally concentrated (Gomez et al., 2010, Mosenkov et al., 2019), which makes this explanation even more unlikely.

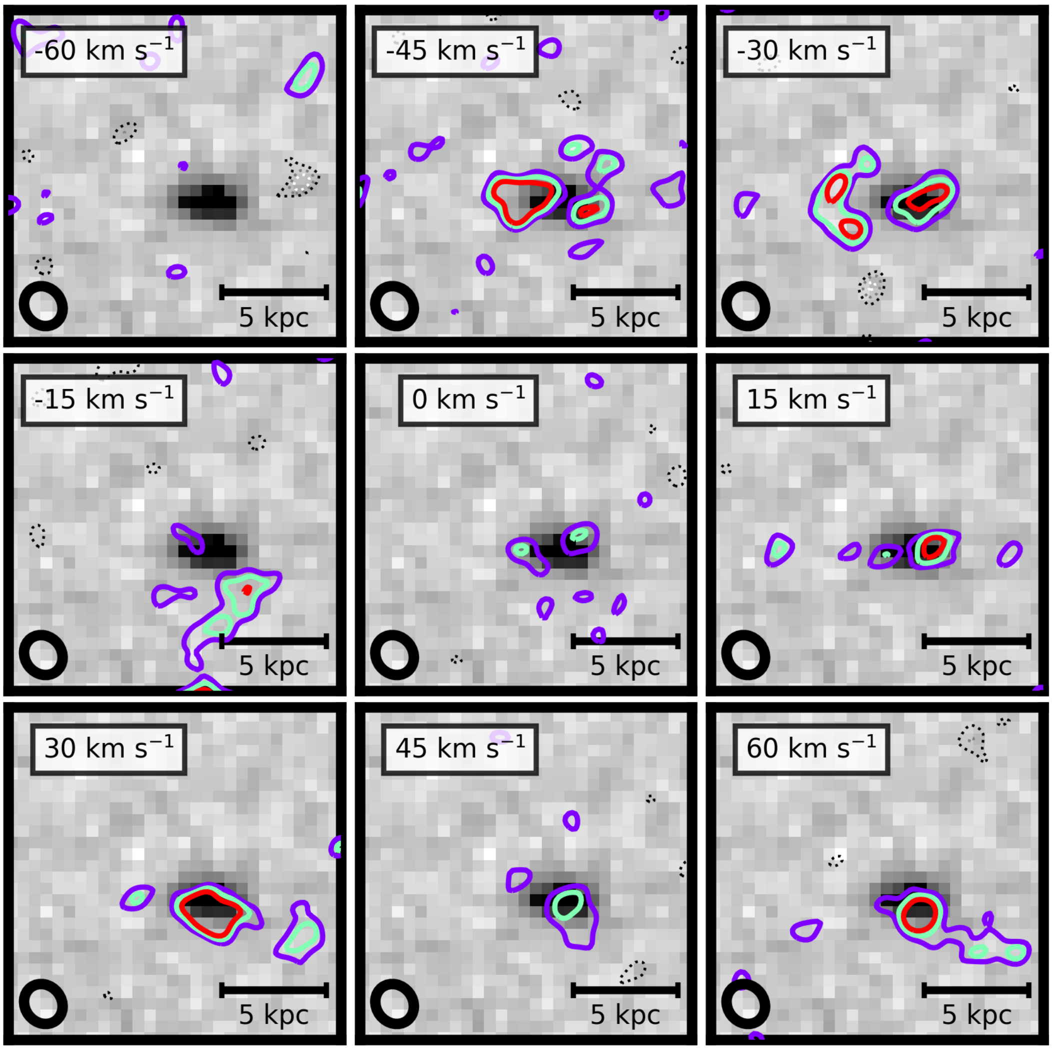

FIGURE 2.6: Channel Map for ± 60 km s^{-1} around the central emission.

As suggested by Fujimoto et al. (2019), it is possible that [CII] haloes are produced by multiple clumps which could be either in-falling satellites or outflowing gas. However, we only find an extended diffuse emission, with no signs of bright clumps, at the resolution of our observations (0.3" $\sim$ 2 kpc). This implies that if indeed the extended emission is produced by clumps, they would have to be numerous and significantly smaller than 2 kpc.

A point of particular interest in the continuum emission in Figure 2.3, is the presence of a Southern continuum extension, extending well beyond the bounds of the [CII] emission. This could possibly correspond to an interloper, which would result in the [CII] emission being redshifted out of the band, or alternatively this dust emission might be a merger remnant which would imply that HZ7 is a late stage merger. This would be in agreement with the disturbed velocity field and dispersion map in Figure 2.2 as well as the -15 km

s^{-1} panel in Figure 2.6. However, while both of these potential scenarios would be in agreement with the existence of this southern continuum emission, they are both unlikely as the probabilities of their occurrences are rare. It is entirely possible that the continuum data does not have a high enough SNR in order to make any firm deductions. Higher S/N observations of the continuum would be needed in order to fully investigate its contribution

Another explanation for the extend [CII] emission is gas stripping due to tidal interactions which would exist in a merging system. In this case, the [CII] would be excited by shocks, as has been observed at low redshifts by Appleton et al. (2013), in Stephan's Quintet. This explanation is supported by the ratio between the [CII] and FIR emission in the system. Barisic et al. (2017) calculates an upper FIR limit of $\log\left(L_{\mathrm{FIR}}/L_{\odot}\right) < 10.35$, resulting in a lower limit ratio $\log\left(L_{[\mathrm{CII}]}/L_{\mathrm{FIR}}\right) > 1.5$, which would imply shock-enhanced [CII] emission according to Appleton et al. (2013). A similar physical argument is made in Ginolfi et al. (2020a), at higher redshifts ($z \sim 4.57$). This physical explanation of the existence of a [CII] halo further supports the possibility that HZ7 is a merging system.

2.5 Summary and Conclusions

HZ7 is a so-called "normal" galaxy at $z = 5.25$ for which the physical properties (morphological and kinematical) are still not well understood. We have presented new high resolution [CII] line emission observations with ALMA of HZ7 with the aim of exploring its kinematics and morphology.

HZ7 is unequivocally not a simple rotating disk galaxy and this has been shown by the [CII] velocity field and the [CII] dispersion map (middle and bottom panels of Figure 2.2). The overall structure of both the moment-1 and moment-2 maps suggest that HZ7 could possibly be a merger. This is further supported by the southern continuum emission in Figure 2.3. Determining whether or not the system is actually a merger would require further inspection and study, including follow-up high resolution ALMA observations.

We have also presented strong evidence of the existence of a [CII] halo which surrounds the UV emission. Whilst the existence of such haloes has been suggested (Fujimoto et al., 2019, Ginolfi et al., 2020a), this is amongst the first clear, high resolution, direct observational evidence. The [CII] emission has an effective radius of $3.60^{+0.49}_{-0.64}$ kpc, for a free Sérsic index (and an effective radius of $3.07^{+0.23}_{-0.25}$ for a fixed Sérsic index of 1) whilst the average UV emission amongst the three filters ~ 1.4 kpc—indicating a [CII] halo extending 3.3 times the UV emission.

This result provides theoretical models with another example in order to explain the physical process which might result in the existence of such a halo, as contributing to the growing number of case studies of [CII] haloes around "normal" galaxies at these redshifts. This could imply an important and essential role in the galactic evolution of ordinary galaxies.

Follow-up observations of this system as well as other similar systems will be essential in determining the evolutionary aspects of ordinary galaxies in epoch of reionization. One such project which will help place this particular galaxy in context of other "normal" galaxies is ALMA-CRISTAL survey [3] which is a cycle 8 ALMA program which will observe 19 similar galaxies in [CII].

---

[3] `https://www.alma-cristal.info/home`

Chapter 3

Overdensity of LAEs in a 3 deg^2 field around a $z = 6.9$ quasar but lacking LAEs within 5 pMpc: potential evidence of negative feedback in the quasar vicinity?

3.1 Introduction

Several high-redshift quasars have been identified within the Epoch of Reionization (Fan et al., 2023, 2006, Venemans et al., 2007, 2013, Wang et al., 2021, Willott et al., 2010) which is believed to have ended at $z = 5.3$ (Bosman et al., 2022). In many cases, the super massive black holes at the core of these quasars have masses in excess of $10^9\ M_\odot$ (e.g., Eilers et al., 2023, Farina et al., 2022, Mazzucchelli et al., 2023, Yang et al., 2023) but have had a relatively short amount of time (less than 1 Gyr) for accreting the large amounts of material needed to build up those masses (Inayoshi et al., 2020, Volonteri, 2012). This can only be feasible if these high-redshift quasars are located within very dense regions of the early Universe (Decarli et al., 2019). Simulations have indeed shown that we should expect to find these very massive SMBHs—and by analogy, quasars—in the most massive dark matter haloes at $z > 6$ and these should be traced by highly clustered galaxies (Angulo et al., 2012, Costa et al., 2014).

Observationally confirming the predictions made by simulations requires searching for galaxies around high-redshift quasars and comparing the densities found to blank fields (i.e., regions of sky without any quasars at similar redshifts that provide an estimate of the average density of the Universe). Yet this is difficult to do: whilst we can observe the very bright quasar at high-redshifts with relative ease, identifying the companion galaxies tracing the overdensity is a lot more difficult because of how much fainter they are.

The main observational strategy used to search for galaxies around quasars of a known redshift is photometrically identifying either Lyman-break galaxies (LBGs, e.g., Husband et al., 2013, Kim et al., 2009, Morselli et al., 2014, Utsumi et al., 2010, Zewdie et al., 2023) or Lyman-α emitters (LAEs, e.g., Bañados et al., 2013, Goto et al., 2017, Mazzucchelli et al., 2017a, Ota et al., 2018) by using broadband (FWHM $\sim$ 1000 Å) photometry for the former and a combination of broad- and narrowband (FWHM $\sim$ 100 Å) photometry for the latter. However, results across multiple studies using these techniques to estimate the environmental densities around these high-redshift quasars have resulted in varying, and often conflicting, results. Some studies have detected overdense regions around quasars (Balmaverde et al., 2017, Capak et al., 2011, Decarli et al., 2019, Husband et al., 2013, Mignoli et al., 2020, Morselli et al., 2014, Utsumi et al., 2010, Zheng et al., 2006) while others have not (Bañados et al., 2013, Goto et al., 2017, Mazzucchelli et al., 2017a, Simpson et al., 2014, Stiavelli et al., 2005, Willott et al., 2005). Sometimes finding conflicting results for the same targets: e.g., SDSS J1030+0524 where Willott et al. (2005) did not find an overdensity but Decarli et al. (2019), Mignoli et al. (2020), Stiavelli et al. (2005) did; likewise for SDSS J1048+4637 and SDSS J1148+5251 where Willott et al. (2005) and Kim et al. (2009) didn't find overdensities but later Morselli et al. (2014) did. In order to explain these contrasting results, observational biases need to be considered.

For example, consider the difference in redshift resolution (Δz) between LBGs and LAEs. LBG searches generally have $\Delta z \sim 1$ (Mazzucchelli et al., 2017a) when using three broadband filters (the majority of LBG searches around high-z quasars), and even though this can be lowered with more filters and unique set-ups (to about $\Delta z \sim 0.3$; García-Vergara et al., 2017), LAE searches, because of the small wavelength range of the narrowband, have resolutions of $\Delta z \sim 0.1$ (Hu et al., 2019), making LAEs a more reliable method. Galaxies that are found using the LBG technique might not actually be associated with the protocluster environment (Bañados et al., 2013).

Another observational effect, which is often not considered when searching for overdensities around quasars, is the method used to determine the quasar redshift. Most studies adopted quasar redshifts that have been measured been using rest-frame UV lines. However, with the advent of ALMA, it became clear that the redshifts from UV can be offset by thousands of km s^{-1} from the host galaxy's systemic redshifts (e.g., Decarli et al., 2018, Díaz-Santos et al., 2021, Schindler et al., 2020). This offset can often be large enough to shift the Ly-α emission outside of a narrowband filter, resulting in false non-detections of overdensities. To date, only Ota et al. (2018), who searched over a 0.2 square degree area, has performed a LAE search using a [CII] redshift instead of rest-frame UV. They did not find an overdensity; it is worth noting that the Ly-α line in their case, was near the edge of their narrowband filter.

The final observational effect which might bias results is the search area; protocluster areas are expected to be on scales of 10 pMpc with cosmic variance on the scale of $\sim 1^\circ$ (18 pMpc at $z = 6.9$), however, most studies have searched areas far smaller than this (Balmaverde et al., 2017, Overzier et al., 2009).

Accounting for these observational biases would require 1) a quasar with a known, non-restframe UV redshift, 2) a telescope with a large FoV, and 3) a narrowband filter at the correct wavelength range. This is exactly the case for the quasar VIK 2348–3054 (Venemans et al., 2013), which has a confirmed [CII] redshift of $z = 6.9018 \pm 0.0007$ (Venemans et al., 2016), and whose Ly-α emission falls within the response of the narrowband filter available for the Dark Energy Camera (DECam; Zheng et al., 2019) on the 4m Blanco telescope at Cerro Tololo Inter-American Observatory (CTIO), which has a 3 square degree FoV.

In this paper we take full advantage of this serendipitous combination of telescope, instrument, and target and perform a LAE search around the quasar VIK J2348–3054, with a bolometric luminosity and black hole mass of 0.43×10^{47} erg s^{-1} and $1.98\times10^{9}\ M_\odot$ respectively (see Mazzucchelli et al., 2017b). The remainder of the paper is organized as follows: Section 2 describes the observational setup adopted to perform the search. We present the results in Section 3, and in Section 4 we discuss the implications of these results and offer an explanation as to the current tension within the literature. We present our conclusions in Section 5.

Throughout this paper we adopt a vanilla, flat ΛCDM cosmology with $\Omega_m = 0.3$, and $H_0 = 70$ km s^{-1} Mpc^{-1}. At $z = 6.9$ the Universe is 0.753 Gyr old and the transverse scales are 24 arcseconds/cMpc and 189 arcseconds/pMpc.

3.2 Observations

We observed the area around VIK J2348–3054 with DECam housed on the 4m Blanco telescope at the CTIO (PROPID: 2021B-0905). The observing run was split into two parts: the first took place over four half-nights from the UT 2021-08-30 to the UT 2021-09-03, while the second occurred over two half-nights on UT 2021-10-20 and 2021-10-21.

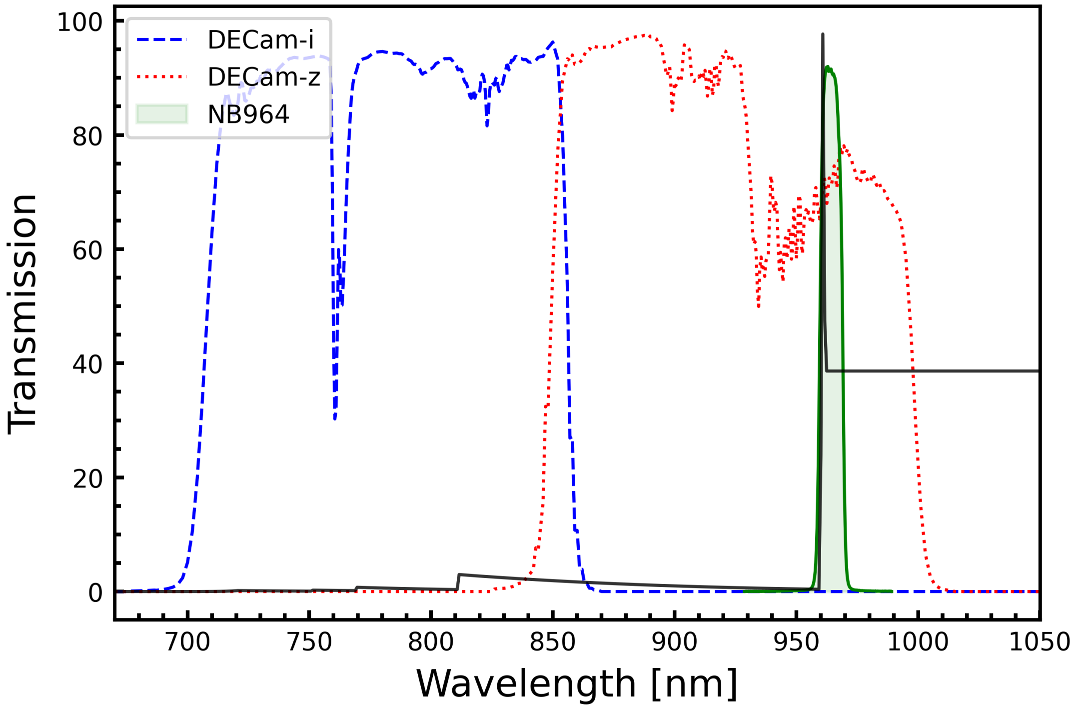

Figure 3.1: Transmission curves for the filters used in this work. The narrowband (NB964 filter) is represented by a solid green line and the two broadbands are represented as the blue and red dashed lines, for i and z, respectively. The LAE synthetic spectrum is shown as the solid black line.

From the combined six half-nights of observations we obtained integrations of 5.8, 8.6, and 14.2 hours in the i-band (λ_c = 7840 Å; $\Delta\lambda$ = 1470 Å), z-band (λ_c = 9260 Å; $\Delta\lambda$ = 1520 Å), and NB964 narrowband (λ_c = 9640 Å; $\Delta\lambda$ = 94 Å) respectively. The filter transmission curves are shown in Figure 3.1.

This particular choice of filters allow us to search for LAEs within a redshift range of $6.89 < z < 6.97$, making it ideal for a search around VIK J2348–3054 at $z = 6.9$ (Venemans et al., 2016). Because DECam has 64 individual CCDs there are numerous chip gaps. To account for this and obtain the best possible data quality, we implemented a dithering pattern during the observations, randomly shifting the poiting position for each set of exposures.

Each band was stacked using the DECam community pipeline (Valdes et al., 2014), then astronomically aligned to the GAIA DR2 catalog (Gaia Collaboration et al., 2018b) and finally trimmed to cover the same area in all bands.

We masked several obvious CCD artifacts which included stellar haloes and image "ringing" i.e., clusters of two or three unrealistically bright and/or negative pixels, by eye on a case by case basis. We also mask noisy edges by creating a ds9 region within the borders of the combined images. The final usable field of view (FoV) is 2.87 deg^2. At the redshift of VIK J2348–3054 this area is equivalent to 1034 pMpc^2

3.2.0.1 Photometric Calibration

Previous DECam N964 filter calibrations have often used Spectral Energy Distribution (SED) fitting of bright stars (either A, B or F0 stars) identified in the field (Hu et al., 2019, Khostovan et al., 2020, Wold et al., 2019a). However, Wold et al. (2019a) showed that calculating zero points using a best-fit straight line is equivalent to SED fitting if there is a linear relationship between the $z - NB964$ and $z - y$ colors, for bright, point like sources. In particular isolated stars. We show this relationship for our data in Figure 3.2 by plotting the color-color diagram of sources which were identified as stars by SExtractor, and had z-band, y-band and i-band colors in the Panoramic Survey Telescope and Rapid Response System (Pan-STARRS1) first data release (Chambers et al., 2016). We therefore photometrically calibrated the N964 filter using the method by Wold et al. (2019b, 2022), assuming a linear relation between the PS1 and DECam magnitudes for point sources:

$$z_{ps1} = \mathrm{N964} + \alpha\,(z_{\mathrm{ps1}} - y_{\mathrm{ps1}}) + \mathrm{ZPT}, \tag{3.1}$$

where z_{ps1} and y_{ps1} are the z and y Pan-STARRS1 magnitudes respectively, N964 is the narrowband magnitude in DECam, and α and ZPT are the slope and zero point which are needed to transform the magnitudes. The α and ZPT values are solved by fitting a best-fit straight line, shown in Figure 3.2. The shaded area represents the 1σ value of the linear fit.

The photometric transformations for the DECam broadband filters are available via the Dark Energy Survey data management (Abbott et al., 2021) who used (amongst other surveys) the Pan-STARRS1 survey [1]. Following their work, we photometrically calibrated the broadband filters using the following transformations:

$$z_{\mathrm{DECam}} = z_{\mathrm{ps1}} - 0.114\,(r_{\mathrm{ps1}} - i_{\mathrm{ps1}}) - 0.010 \tag{3.2}$$

$$i_{\mathrm{DECam}} = i_{\mathrm{ps1}} - 0.155\,(r_{\mathrm{ps1}} - i_{\mathrm{ps1}}) + 0.015. \tag{3.3}$$

The offset between the instrumental DECam magnitudes and the converted Pan-STARRS1 magnitudes is used as the zero point.

---

[1] https://des.ncsa.illinois.edu/releases/dr2/dr2-docs/dr2-transformations

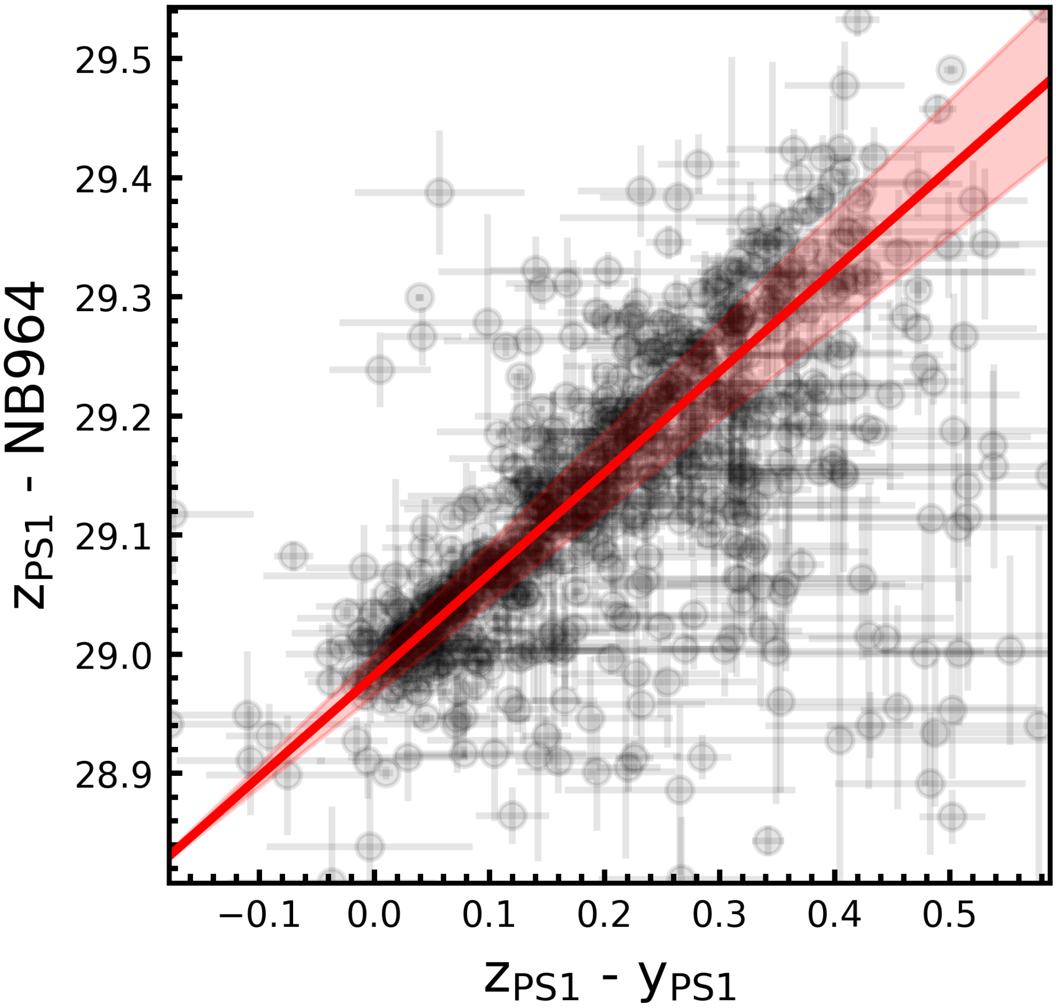

FIGURE 3.2: Color-color diagram of stars identified in the DECam image. Red line is a straight-line fit, indicating a linear relationship.

3.2.0.2 Photometry

We used SExtractor (Bertin & Arnouts, 1996) to create the source catalog for each DECam image. Because we are interested in LAEs which must necessarily be detected in the narrowband, we use it as the detection image and then run SExtractor in dual mode with 2" diameter apertures on the broadband images. This choice of aperture size is based on previous observations using the DECam instrument by Hu et al. (2019) who noted that this allows a large amount of flux to be observed whilst at the same time minimizing contamination from nearby sources. At the same time, this aperture choice is also larger than our worst seeing—1.47" for the narrowband.

The DECam pipeline generates an inverse variance image which takes into account pixel to pixel variations with respect to their uncertainties. We passed this weight-image as a parameter to SExtrator to estimate the photometric errors.

If a source was not detected in either broadband image, we adopted a 1σ limiting magnitude and use this as a lower limit (27.14 for the i-band and 27.00 for the z-band).

3.2.0.3 Depth

The limiting magnitudes were determined by fitting an exponential function to the relationship between detected sources' magnitudes and their signal-to-noise ratios (SNRs), given by:

$$SNR = \frac{2.5}{\ln(10)\, u\, (\mathrm{mag})}, \tag{3.4}$$

where $u\,(\mathrm{mag})$ is the photometric uncertainty, corresponding to the `MAGERR_APER` value from SExtractor.

We found that the limiting 5σ magnitudes for the narrowband, i-band, and z-band were 24.65, 25.40, and 25.25 respectively, for 2" apertures.

3.2.1 DECam Observations of the CDFS LAGER field

We use the CDFS LAGER field, observed by Hu et al. (2019), for comparison since it does not contain a known quasar or any other feature that would make it unusual at the redshift of VIK J2348–3054. This field was observed with the same telescope, instrument, and filters that we used to search for LAEs around the VIK J2348–3054. We utilize the same images used by Hu et al. (2019). The CDFS images have several CCD artifacts as well as large areas of low SNR, mainly within the chip gaps due to insufficient dithering. We manually masked CCD artifacts and automatically masked the chip gap regions in each image using the corresponding weights image. The effective area available for source detection after masking was ~ 1.56 deg^2, or ~ 570 pMpc^2 at the redshift of VIK J2348–3054.

We photometrically calibrate the CDFS images with the same method used for our DECam data.

While the narrowband depths are similar between the observations around VIK J2348–3054 and CDFS, the broadbands in CDFS are about 2 magnitudes deeper (see Hu et al., 2019), so it is necessary to degrade the CDFS photometry to mimic our depths. To do this we create a source catalog using SExtractor in the same way that we did for our data and then, to account for the worse error that we expect for an image of lower depth, we assign new errors for every detected source based on the fitted exponential functions from the depth calculations for our data (discussed §2.1.3) resulting in a degraded magnitude error, $\sigma_{\mathrm{degraded}}$. To account for the expected scatter due to a lower depth image, we

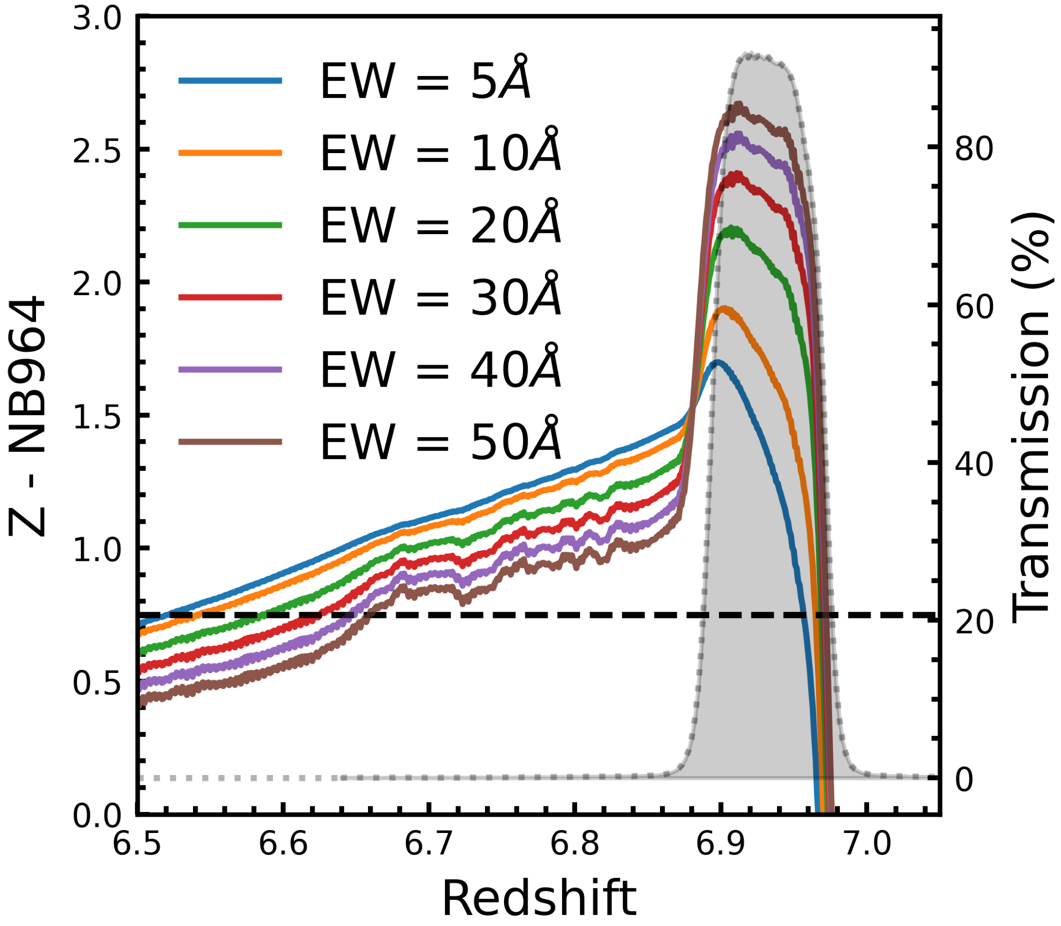

FIGURE 3.3: Predicted Z-NB964 color of a Ly-α emitter for redshifts ranging from 6.5 to 7 for varying equivalent widths. The dashed line indicates the Z-NB964 color selection criteria that we have adopted and the shaded region shows the NB964 filter profile.

randomly assign a source magnitude which is drawn from a normal distribution with a mean equal to the magnitude determined in the CDFS image and a standard deviation equal to $\sqrt{\sigma^2_{\rm degraded} - \sigma^2_{\rm CDFS}}$, where $\sigma_{\rm CDFS}$ is the original magnitude error determined by SExtractor in the CDFS image.

3.2.2 Selection Criteria

A typical LAE has very strong Ly-α emission and a faint continuum (Ouchi et al., 2020). We plot a synthetic LAE spectrum at the redshift of VIK J2348–3054, along with the filter curves in Figure 3.1. The standard IGM extinction from Madau (1995) was assumed. The line was made by assuming a 200 km s^{-1} FWHM value and an equivalent width of 50 Å. The luminosity was derived using the $\alpha = -1.5$ luminosity function, derived from a combination of UDS + COSMOS + SA22, reported in Matthee et al. (2015). As expected, the strong Ly-α emission is contained within the NB964 filter, with practically no continuum in the i-band. And the z-band flux is dominated by the source continuum. Given this, we adopt a similar selection criteria to that used by Bañados et al. (2013) and Mazzucchelli et al. (2017a), namely:

$$|z - NB| > 2.5\sqrt{\sigma_z^2 + \sigma_{NB}^2}, \tag{3.5}$$

$$z - NB > 0.78, \tag{3.6}$$

$$i - z > 1, \tag{3.7}$$

$$\mathrm{SNR(i)} < 2. \tag{3.8}$$

Note that when written like this, the requirement (Eq. 5) deviates at faint magnitudes from a strict lower limit in the f_{NB}/f_z flux ratio and in practice ends up requiring a detection in the z-band. This makes the color selection significantly more robust against interlopers.

We also require that the bright Ly-α emission within the narrowband outshines the continuum (Eq. 6). Figure 3.3 shows the estimated z-NB964 color over a range of redshifts for LAEs with different equivalent widths. And for all of them, the z-NB964 color is above 1.3. The significance criterion implies that a source with a color of 1.3 requires a corresponding error of < 0.52. Therefore we choose a $z - NB964$ threshold of $> 1.3 - 0.52 = 0.78$ mag.

Finally, we require a significant identification of the continuum break short of Ly-α (Eq. 7). Figure 3.1 shows clearly that the expected continuum emission on the blue side of the Ly-α line is very weak due to the IGM absorption, whilst the continuum on the red side should still be detected in the z-band. Therefore we choose a $i - z$ color > 1 as well as require SNR(i) < 2 (Eq. 8).

To further justify our selection we take the synthetic LAE spectrum from Figure 3.1, and derive the expected colors using the python package `synphot` for different redshift values, ranging from 5 to 9. This color-color track is shown in Figure 3.4 and justifies our color selections, demonstrating that these choices are optimal to select select Ly-α emitters around the quasar redshift.

The color-color plot of all the detected sources in our field is shown in Figure 3.5. The black points are the detected sources, the red dashed lines indicated the color selection criteria, and the red points highlight the LAE candidates which meet the selection criteria. The green box highlights the color selection for LAEs.

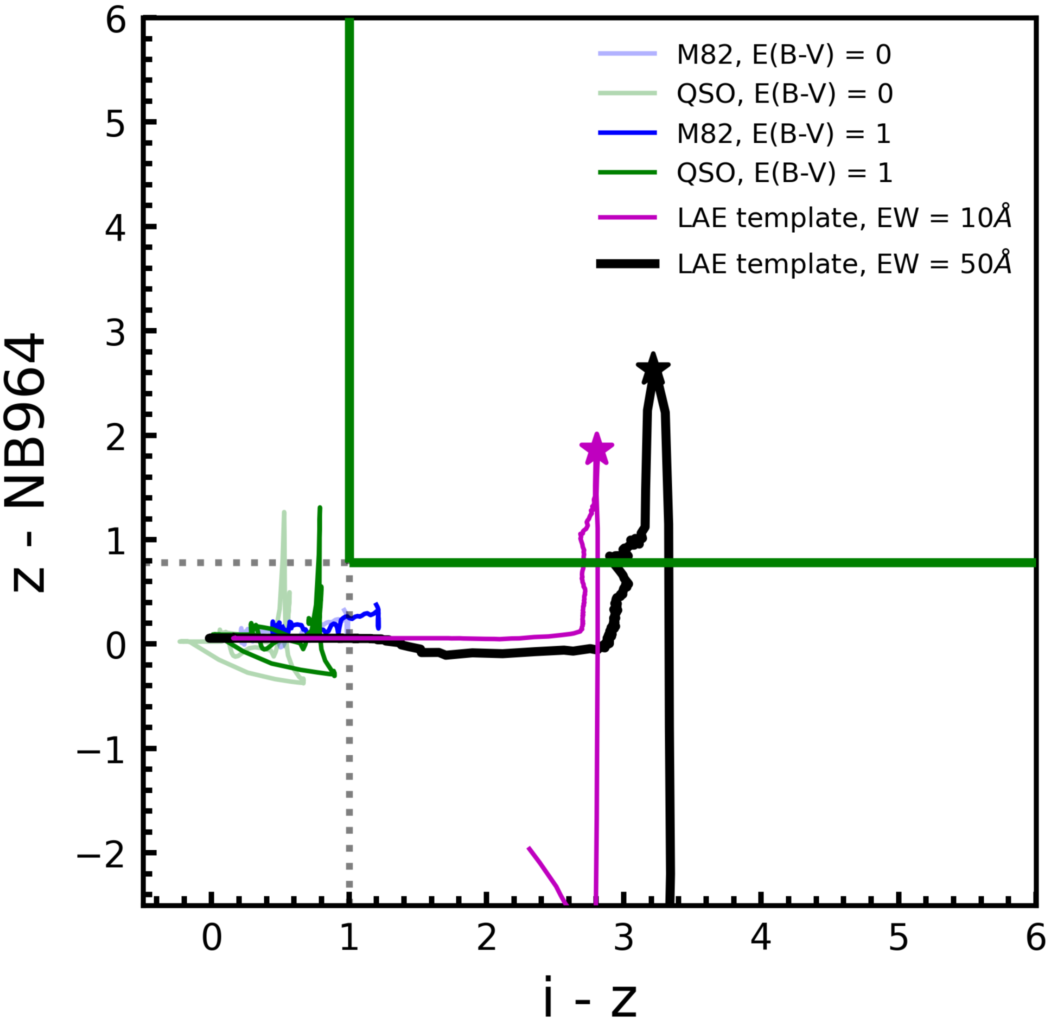

FIGURE 3.4: Color-color values for a synthetic LAE for different redshifts, ranging from $z = 5$ to $z = 9$. Dashed lines show our color selection criteria for LAEs at $z \sim 6.9$. The purple star indicates the redshift of VIK J2348–3054 at $z = 6.9$.

3.3 Results

3.3.1 LAE Candidates

We find 39 sources sources in the VIK J2348–3054 field which meet our selection criteria: 38 LAE candidates as well as the quasar itself. The 20 pix × 20 pix (10.8" × 10.8") postage stamp cut outs of all the candidates are presented in Figure 3.6. We also indicate the magnitudes in the respective bands as well as their SNRs. While all candidates formally meet our selection criteria (see §2.3), we do note that three candidates (LAE-25, LAE-30, and LAE-38) seem to have obvious i-band detections despite SExtractor assigning them very low SNR values.

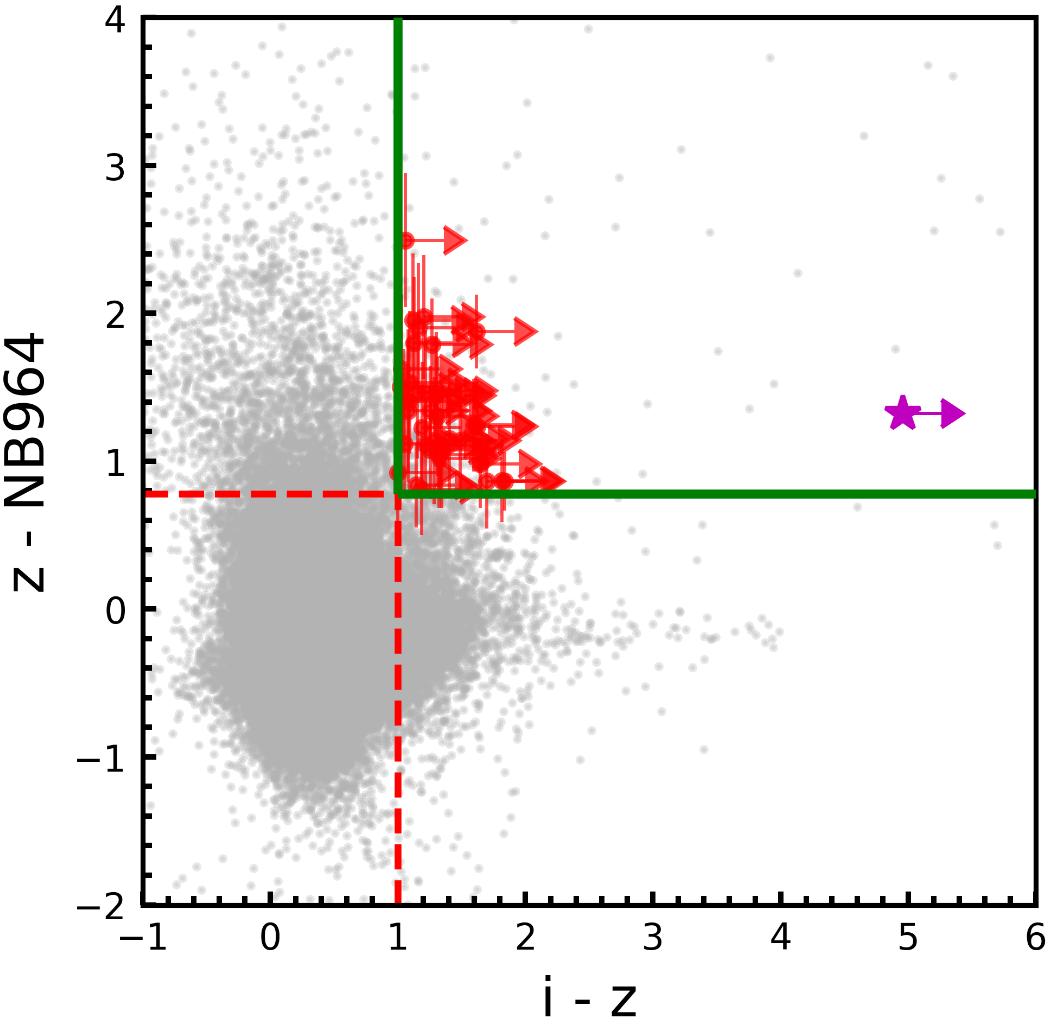

Figure 3.5: Color-color diagram. Red points show the LAE candidates in the field of VIK J2348–3054. Black points show all the sources that were identified with SExtractor.

By contrast, only two candidates were identified in the CDFS images after the photometry degradation (see §2.3). Their 20 pix × 20 pix (10.8" × 10.8") postage stamp cut outs are presented in Figure 7.

Our candidate properties are presented in Table 3.1, including the candidate positions, their angular separations from VIK J2348–3054, comoving and proper distances, i-band, z-band, and NB964 magnitudes, Ly-α luminosities, and derived star formation rates (see sections 3.2 and 3.3).

The on-sky distribution of the LAE candidates around the quasar can be seen in Figure 8

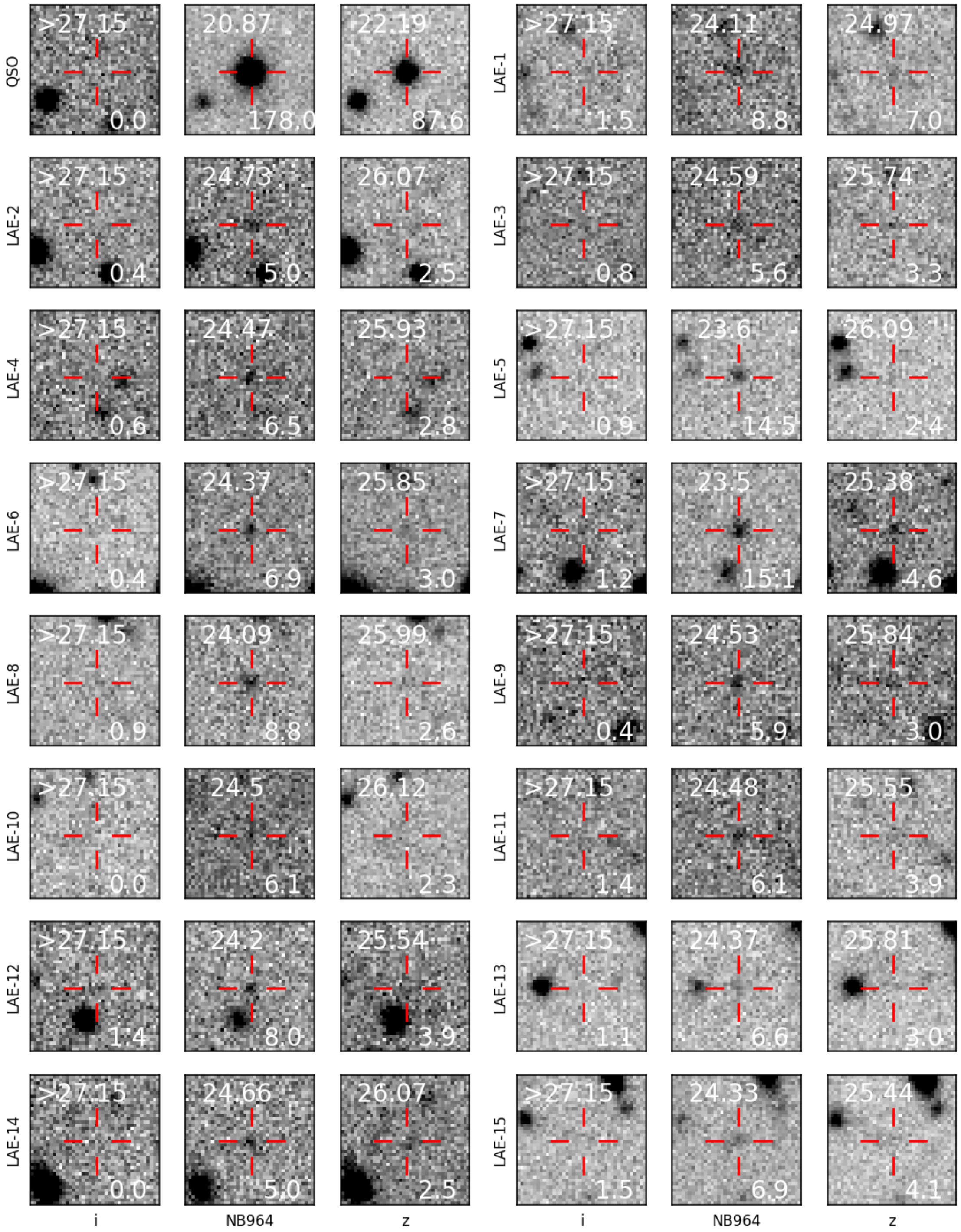

FIGURE 3.6: LAE candidate 20 pix × 20 pix (10.8” × 10.8”) cutouts, identified in our DECam data. The values in the top of each postage stamp indicate the AB magnitudes in the i, NB964, and z bands whilst the bottom show the SNR values in those respective bands.

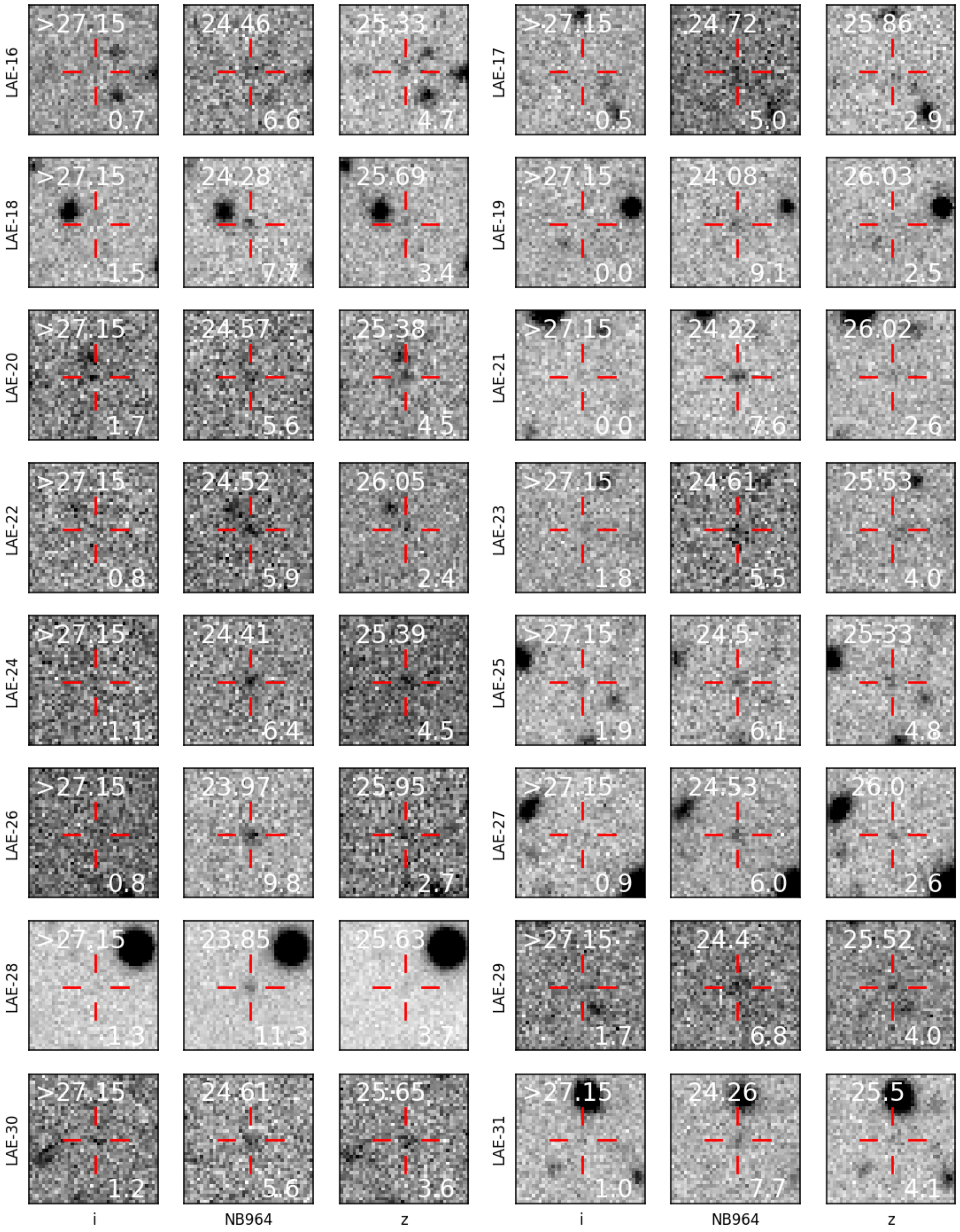

Figure 6 (Cont.)

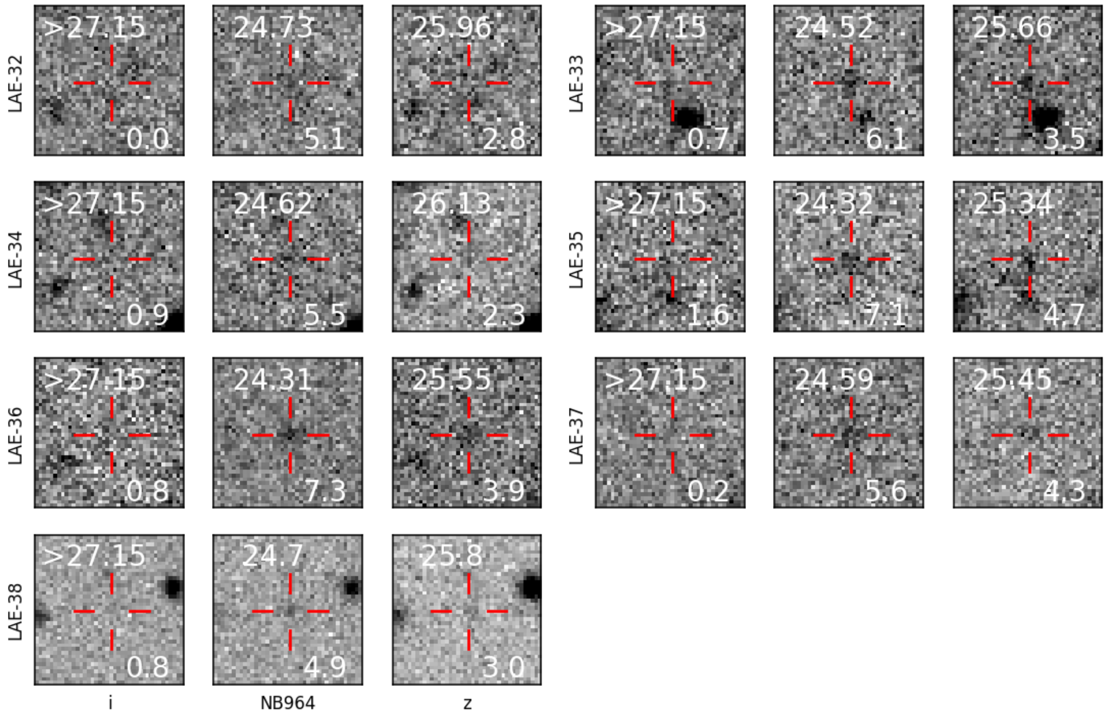

Figure 6 (Cont.)

3.3.2 Estimation of Ly-α Luminosities

We follow the same method used by Hu et al. (2019) to determine the Ly-α luminosities. Specifically, we use the following equation to estimate $f_{\rm line}$,

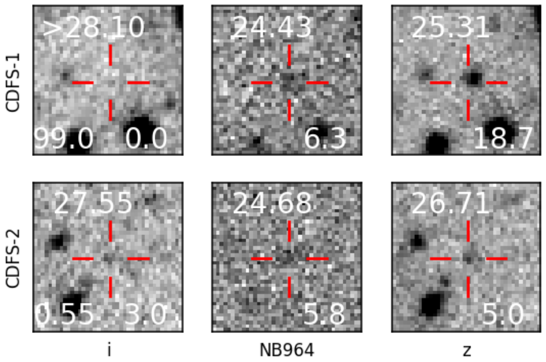

Figure 7: LAE candidate 20 pix × 20 pix (10.8” × 10.8”) cutouts, identified in the degraded CDFS data. The values in the top of each postage stamp indicate the AB magnitudes in the i, NB964, and z bands whilst the bottom show the SNR values in those respective bands.

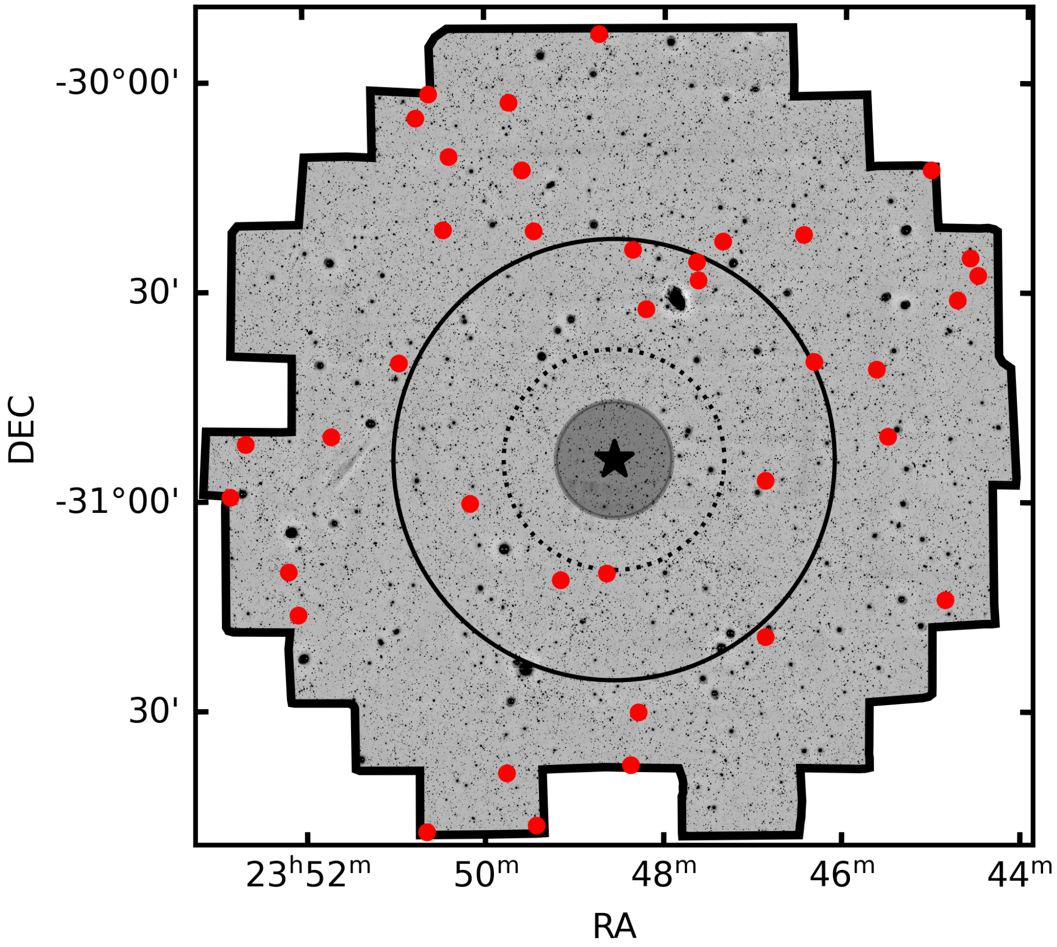

Figure 8: LAE on-sky distribution around the quasar. The black outline is the area used to identify LAE and is slightly smaller than the full DECam FOV. The star at the image center is the quasar location. The shaded region shows the proximity zone determined by Mazzucchelli et al. (2017b). The inner and outer rings highlight 5 pMpc and 10 pMpc from the quasar respectively, with the later being the maximum scale of an overdensity that we expect from Overzier et al. (2009).

$$k_x \bar{f}_\nu = \int \left(f_{\text{line}} + f_{\text{cont}}\right) T_x(\lambda) d\lambda \tag{3.9}$$

$$= \int f_{\text{line}} T_x(\lambda) d\lambda + \int f_{\text{cont}} T_x(\lambda) d\lambda, \tag{3.10}$$

where $T_x(\lambda)$ is the transmission function of filter x (in our case x is either NB964 or the z-band), $\bar{f}_\nu$ is the detected flux density, and k_x is a constant defined as:

$$k_x \equiv c \frac{\int T_x(\lambda) d\lambda}{\bar{\lambda}_x^{\,2}}, \tag{3.11}$$

TABLE 3.1: Names, Coordinates, projected distances from the quasar, i-band, z-band, and NB964-band magnitudes, Ly-α luminosities, and star formation rates for the LAE candidates identified in this work

ID	R.A.	Dec.	θ	r_c	r_p	i	z	NB964	$L_{\mathrm{Ly}\alpha}$	SFR
	(J2000.00)	(J2000.00)	(deg)	(cMpc)	(pMpc)				$\times10^{42}$ (ergs s^{-1})	($M_\odot$ yr^{-1})
QSO	23:48:33.33	-30:54:10.23	0.00	0.00	0.00	>27.15	22.19 ± 0.05	20.86 ± 0.01	239.9 ± 2.2	148.1 ± 1.4
LAE-1	23:50:39.46	-31:47:26.41	0.99	149.20	18.89	>27.15	24.97 ± 0.23	24.11 ± 0.12	12.1 ± 2.3	7.5 ± 1.4
LAE-2	23:49:25.39	-31:46:34.95	0.89	133.93	16.95	>27.15	26.07 ± 0.74	24.73 ± 0.22	6.8 ± 2.3	4.2 ± 1.4
LAE-3	23:49:45.53	v31:39:01.46	0.79	118.57	15.01	>27.15	25.74 ± 0.10	24.59 ± 0.19	7.7 ± 2.3	4.8 ± 1.4
LAE-4	23:48:22.23	-31:37:53.92	0.73	109.47	13.86	>27.15	25.93 ± 0.06	24.46 ± 0.17	8.7 ± 2.2	5.4 ± 1.4
LAE-5	23:48:17.08	-31:30:18.94	0.61	90.77	11.49	>27.15	26.09 ± 0.08	23.59 ± 0.07	19.4 ± 2.2	12.0 ± 1.4
LAE-6	23:46:51.65	-31:19:29.93	0.56	83.48	10.57	>27.15	25.85 ± 0.13	24.37 ± 0.16	9.5 ± 2.3	5.9 ± 1.4
LAE-7	23:52:04.95	-31:16:20.60	0.84	126.08	15.96	>27.15	25.38 ± 0.09	23.50 ± 0.07	21.2 ± 2.3	13.1 ± 1.4
LAE-8	23:44:51.34	-31:14:01.78	0.86	128.78	16.30	>27.15	25.99 ± 0.03	24.08 ± 0.12	12.4 ± 2.3	7.6 ± 1.4
LAE-9	23:49:09.11	-31:11:23.68	0.31	47.13	5.97	>27.15	25.84 ± 0.18	24.53 ± 0.18	8.2 ± 2.3	5.1 ± 1.4
LAE-10	23:48:38.18	-31:10:25.49	0.27	40.72	5.15	>27.15	26.12 ± 0.13	24.49 ± 0.18	8.5 ± 2.3	5.2 ± 1.4
LAE-11	23:52:11.44	-31:10:09.82	0.82	123.43	15.62	>27.15	25.55 ± 0.02	24.47 ± 0.18	8.6 ± 2.4	5.3 ± 1.5
LAE-12	23:50:09.67	-31:00:28.43	0.36	53.98	6.83	>27.15	25.54 ± 0.06	24.20 ± 0.14	11.1 ± 2.3	6.9 ± 1.4
LAE-13	23:52:50.08	-30:59:23.05	0.92	138.21	17.50	>27.15	25.81 ± 0.10	24.37 ± 0.16	9.5 ± 2.4	5.9 ± 1.5
LAE-14	23:46:52.33	-30:57:07.02	0.36	54.65	6.92	>27.15	26.07 ± 0.05	24.66 ± 0.22	7.3 ± 2.4	4.5 ± 1.5
LAE-15	23:52:39.27	-30:51:50.73	0.88	132.02	16.71	>27.15	25.44 ± 99.00	24.32 ± 0.16	9.9 ± 2.4	6.1 ± 1.5
LAE-16	23:51:42.32	-30:50:46.97	0.68	101.71	12.87	>27.15	25.33 ± 99.00	24.46 ± 0.16	8.7 ± 2.2	5.4 ± 1.4
LAE-17	23:45:30.76	-30:50:42.20	0.66	98.31	12.44	>27.15	25.86 ± 0.05	24.72 ± 0.22	6.9 ± 2.3	4.2 ± 1.4
LAE-18	23:45:38.56	-30:41:06.23	0.66	99.34	12.57	>27.15	25.69 ± 0.02	24.28 ± 0.14	10.4 ± 2.2	6.4 ± 1.4
LAE-19	23:50:56.96	-30:40:16.95	0.56	84.55	10.70	>27.15	26.03 ± 0.10	24.07 ± 0.12	12.5 ± 2.3	7.7 ± 1.4
LAE-20	23:46:20.25	-30:40:03.94	0.53	79.67	10.08	>27.15	25.38 ± 0.05	24.57 ± 0.19	7.9 ± 2.3	4.9 ± 1.4
LAE-21	23:48:12.27	-30:32:34.32	0.37	55.15	6.98	>27.15	26.02 ± 0.01	24.22 ± 0.14	10.9 ± 2.4	6.8 ± 1.5
LAE-22	23:44:45.07	-30:31:07.12	0.90	135.50	17.15	>27.15	26.05 ± 0.04	24.52 ± 0.18	8.3 ± 2.3	5.1 ± 1.4
LAE-23	23:47:37.50	-30:28:28.35	0.47	70.89	8.97	>27.15	25.53 ± 0.09	24.60 ± 0.20	7.7 ± 2.3	4.7 ± 1.4
LAE-24	23:44:31.64	-30:27:35.79	0.97	145.88	18.47	>27.15	25.39 ± 0.08	24.41 ± 0.17	9.1 ± 2.4	5.6 ± 1.5
LAE-25	23:47:38.55	-30:25:47.75	0.51	76.79	9.72	>27.15	25.33 ± 0.06	24.49 ± 0.18	8.5 ± 2.3	5.2 ± 1.4
LAE-26	23:44:36.91	-30:25:04.43	0.98	146.42	18.53	>27.15	25.95 ± 0.20	23.97 ± 0.11	13.8 ± 2.3	8.5 ± 1.4
LAE-27	23:48:21.02	-30:24:04.19	0.50	75.52	9.56	>27.15	26.00 ± 0.82	24.52 ± 0.18	8.2 ± 2.3	5.1 ± 1.4
LAE-28	23:47:21.19	-30:22:53.54	0.58	87.27	11.05	>27.15	25.63 ± 0.05	23.84 ± 0.10	15.4 ± 2.3	9.5 ± 1.4
LAE-29	23:46:27.28	-30:21:51.57	0.70	105.43	13.35	>27.15	25.52 ± 0.09	24.40 ± 0.16	9.2 ± 2.3	5.7 ± 1.4
LAE-30	23:49:27.05	-30:21:25.98	0.58	86.77	10.98	>27.15	25.65 ± 0.05	24.61 ± 0.19	7.6 ± 2.3	4.7 ± 1.4
LAE-31	23:50:27.20	-30:21:13.39	0.68	102.61	12.99	>27.15	25.50 ± 0.03	24.26 ± 0.14	10.5 ± 2.3	6.5 ± 1.4
LAE-32	23:45:02.91	-30:12:32.87	1.03	153.76	19.46	>27.15	25.96 ± 0.06	24.73 ± 0.21	6.8 ± 2.2	4.2 ± 1.4
LAE-33	23:49:34.65	-30:12:40.49	0.73	108.83	13.78	>27.15	25.66 ± 0.01	24.52 ± 0.18	8.3 ± 2.2	5.1 ± 1.4
LAE-34	23:50:23.24	-30:10:45.41	0.82	123.58	15.64	>27.15	26.13 ± 0.06	24.62 ± 0.20	7.5 ± 2.3	4.7 ± 1.4
LAE-35	23:50:45.07	-30:05:13.35	0.94	141.41	17.90	>27.15	25.34 ± 0.09	24.32 ± 0.15	9.9 ± 2.3	6.1 ± 1.4
LAE-36	23:49:43.48	-30:03:01.26	0.89	133.31	16.87	>27.15	25.55 ± 0.03	24.31 ± 0.15	10.1 ± 2.3	6.2 ± 1.4
LAE-37	23:50:36.54	-30:01:46.79	0.98	146.80	18.58	>27.15	25.45 ± 0.02	24.58 ± 0.19	7.8 ± 2.3	4.8 ± 1.4
LAE-38	23:48:43.58	-29:53:13.94	1.02	152.41	19.29	>27.15	25.80 ± 0.08	24.70 ± 0.22	7.0 ± 2.4	4.3 ± 1.5

where $\bar{\lambda_x}$ is the central wavelength of filter x and c is the speed of light. For simplicity, we assume that the Ly-α emission line (f_{line}) is a δ-function, centred on the NB964 filter, and the continuum flux (f_{cont}) is a power law spectrum with a slope of -2 and attenuated by the IGM using the model from Madau (1995). Making these assumptions allows us to express Equation (3.10) as:

$$k_x \bar{f}_\nu = f_\alpha T_x(\lambda_\alpha) + C \int \lambda^{-2} e^{-\tau} T_x(\lambda) d\lambda, \tag{3.12}$$

where f_α is the Ly-α flux, C is a constant, λ_α is the Ly-α emission wavelength, and τ is the approximate extinction of Ly-α for a galaxy at a given redshift. When we substitute the narrowband and broadband values into Equation (3.12) we get two equations:

$$k_{NB} \bar{f}_{\nu,NB} = f_\alpha T_{NB}(\lambda_\alpha) + C \int \lambda^{-2} e^{-\tau} T_{NB}(\lambda) d\lambda \tag{3.13}$$

$$k_{BB} \bar{f}_{\nu,BB} = f_\alpha T_{BB}(\lambda_\alpha) + C \int \lambda^{-2} e^{-\tau} T_{BB}(\lambda) d\lambda, \tag{3.14}$$

which we can solve simultaneously for C and f_α, using the latter to determine the Ly-α luminosity ($L_{\mathrm{Ly}\alpha}$).

3.3.3 Star formation rates

We estimate the star formation rates (SFRs) by following the same procedure used by Mazzucchelli et al. (2017a). Using the derived Ly-α luminosities ($L_{\mathrm{Ly}\alpha}$), we can determine Hα luminosities ($L_{\mathrm{H}\alpha}$) by assuming case-B recombination and exploiting the relationship presented in Osterbrock (1989): $L_{\mathrm{Ly}\alpha} = 8.7 \times L_{\mathrm{H}\alpha}$. SFRs can be calculated using the relationship between SFR and $L_{\mathrm{H}\alpha}$ presented in (Kennicutt & Evans, 2012):

$$\log\left(\frac{\mathrm{SFR}_{L_{\mathrm{Ly}\alpha}}}{M_\odot\ \mathrm{yr}^{-1}}\right) = \log\left(\frac{L_{\mathrm{H}\alpha}}{\mathrm{erg\ s}^{-1}}\right) - 41.27. \tag{3.15}$$

3.4 Discussion

3.4.1 Overdensity of LAEs

The surface density of LAEs around VIK J2348–3054 is 13.2 ± 2.2 deg^{-2}, whilst in CDFS we only find a surface density of 1.3 ± 0.9 deg^{-2} to the same depth (see §2.3 for details). This implies that the quasar is sitting within an overdense region with a factor of $\delta = 10^{+5.3}_{-5.9}$, where the uncertainty is derived from the 68% confidence interval, drawn from the ratio of two gamma distributions. We note that given this highly skewed distribution, the probability of the field not being overdense (i.e, the probability that $\delta \leq 1$) is 0.0003 %. To further explore the overdensity factor, we compare the Ly-α luminosity function of our sources against that from the combined CDFS and COSMOS fields from Hu et al. (2019) in Figure 9. For all luminosities we find that the candidates around VIK J2348–3054 have a higher space density than expected from the luminosity function, which again indicates that the quasar lives in an overdense environment. We fit a scaled version of the luminosity function derived in Hu et al. (2019) to our data, i.e., $\delta\Phi\left(L, \Phi^* = -4.19, \alpha = -2.5, L^* = 43.08\right)$ and find that it is $\delta = 14 \pm 3$ times as overdense.

Interestingly, we are only able to find this overdensity due to the large size of our field, as there appears to be a distinct lack of sources in the vicinity of the quasar (see Figure 8).

Figure 10 shows the LAE candidates' radial distribution from the quasar. The blue shaded region represents the average CDFS surface density after being degraded and is

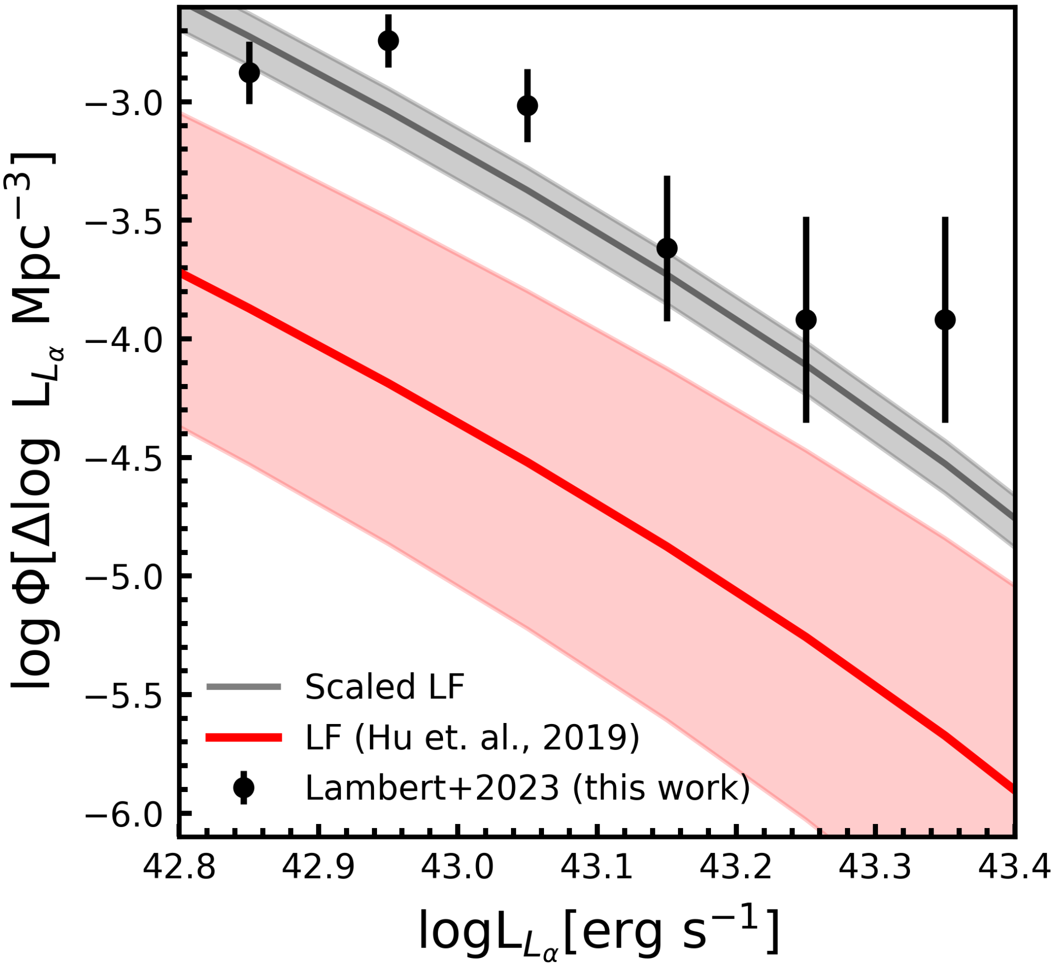

FIGURE 9: The red line shows the selection incompleteness uncorrected luminosity function determined by Hu et al. (2019) using the combined COSMOS and CDFS fields. The black points are the values determined from the LAEs observations in our field.

determined by considering the Poisson single-sided, 1σ upper limit for $n = 2$ (Gehrels, 1986). Non detections ($n = 0$) have been given an upper limit of 1.846 which is again the 1σ upper limit for a single-sided Poisson distribution. Figure 10 also shows the maximum scale of an overdensity, 75 cMpc (9.5 pMpc), expected at this redshift (Overzier et al., 2009) and is also shown as the outer ring in Figure 8. From Figure 10 we can see that the field is overdense throughout all the area covered by our images.

3.4.2 Central suppression of Ly-α emitters

Figure 8 shows the on-sky distribution of LAE candidates. The inner shaded region represents the quasar proximity zone (the theoretical region around a quasar where its UV radiation would have ionized a pure hydrogen ISM; Fan et al., 2006) determined by

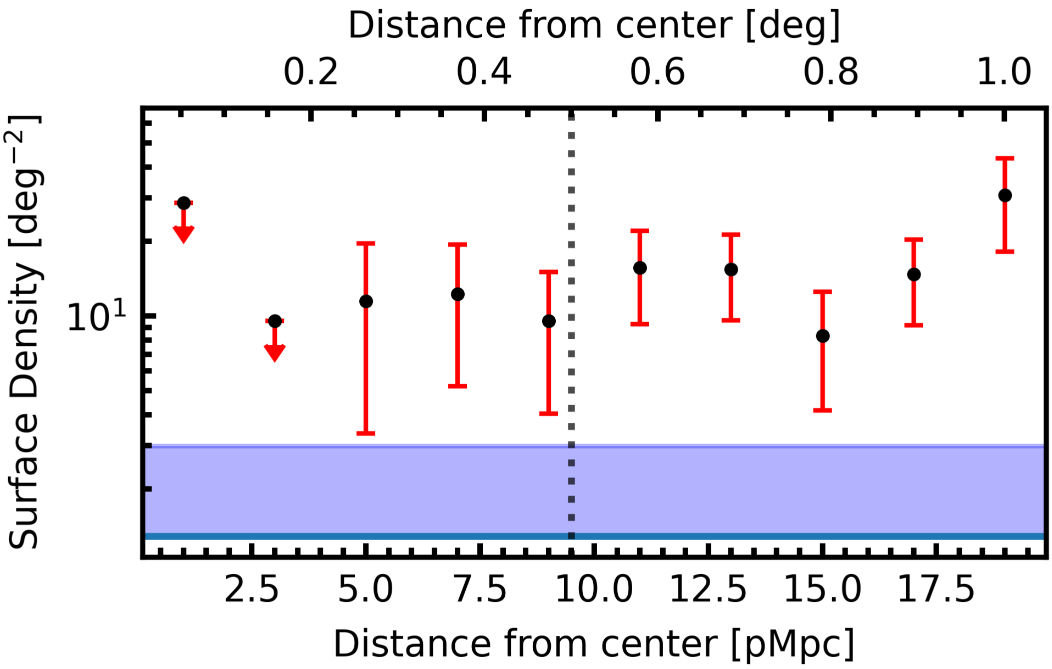

FIGURE 10: Surface density profile as a function of distance from the central quasar. The data were binned using 2 pMpc bins. Red arrows indicate the 1 σ upper limits based on non-detections and assuming a Poisson uncertainty. The blue shaded region is the average upper limit for the degraded CDFS data. The dashed line is the maximum scale of an overdensity found by Overzier et al. (2009).

Mazzucchelli et al. (2017b) to be 2.64 pMpc. The final ring is the largest radius that Overzier et al. (2009) found to contain overdensities. What is striking about the on-sky distribution is the discernible lack of candidates towards the center of the image, around the quasar position (see Figure 10). In fact, the nearest candidate to the quasar is ∼ 0.27° away, i.e., 5.15 pMpc. This distance is indicated as the dashed ring in Figure 8. As the void seems to be centered around the quasar, it is exceedingly unlikely to be driven by interlopers, but instead is a real feature of the quasar environment. If we take the area outside of the maximum overdensity radius, i.e, the region beyond the outer ring in Figure 8 (where we do not expect the quasar to have much, if any, influence) and use this as the true field density, then the Poisson probability of finding the inner region void of LAEs is 1.2% ($\sigma = 2$). However, we do note that this is a ∼ 1% chance around an already rare type of object, and given that we expect an overdensity, finding such an extreme underdensity is most likely much more significant than what we determine through Poison statistics.

We also investigate the on-sky distribution more quantitatively by calculating the two-point angular correlation function, defined by Landy & Szalay (1993) as:

$$\omega(\theta) = \frac{\mathrm{DD}(\theta) - 2\mathrm{DR}(\theta) + \mathrm{RR}(\theta)}{\mathrm{RR}(\theta)}, \tag{3.16}$$

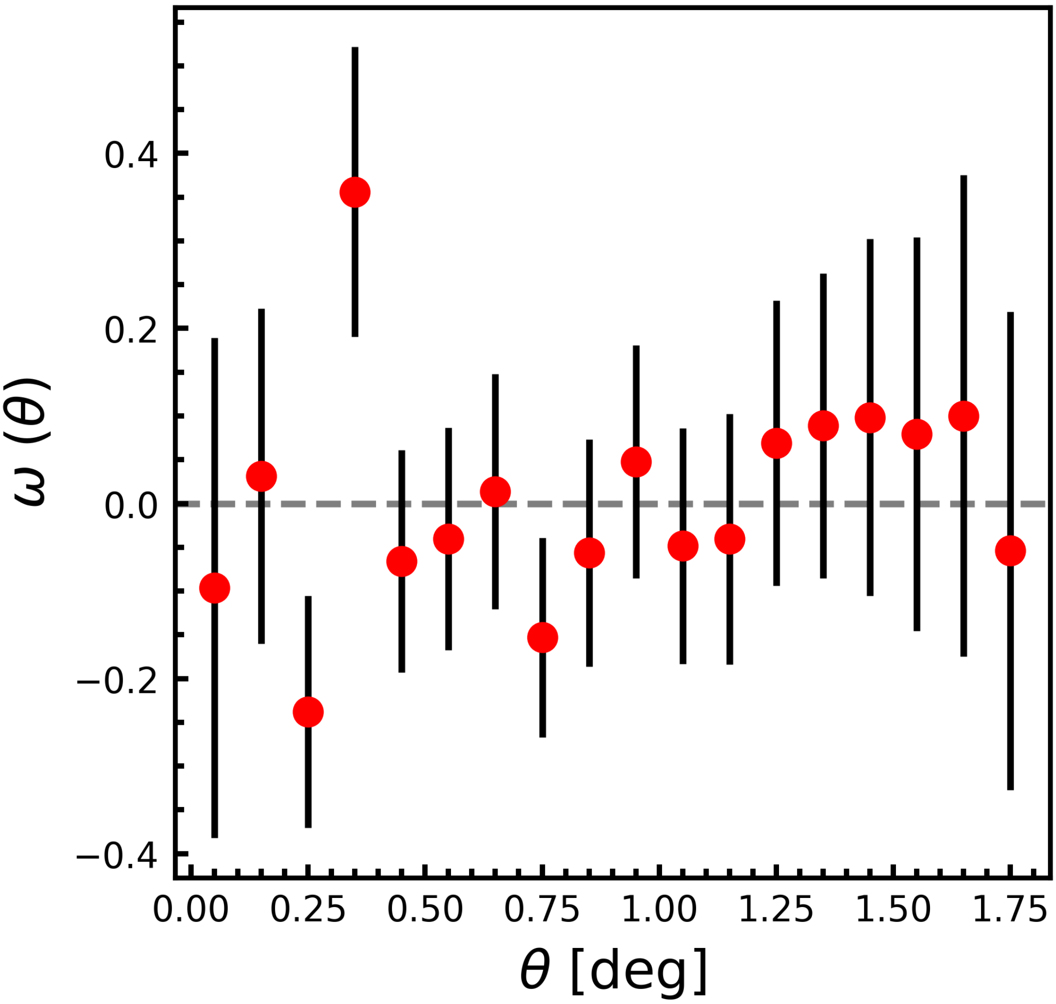

FIGURE 11: Angular two-point correlation function of LAE candidates observed in our field.

with uncertainties

$$\sigma_\omega(\theta) = \frac{1+\omega(\theta)}{\sqrt{\mathrm{DD}(\theta)}}. \tag{3.17}$$

$\mathrm{DD}(\theta)$, $\mathrm{DR}(\theta)$, and $\mathrm{RR}(\theta)$ are the number of galaxy-galaxy, galaxy-random, and random-random pairs, at a given angular separation (θ). We show the angular two point correlation function for our data in Figure 11. It is relatively flat except for a noticeable dip and then peak at $\sim 0.3°$, consistent with the distance between nearest LAE candidate (LAE-10) and the quasar. This suggests that the deviation from a uniform angular correlation is due to the lack of LAEs at the image center.

In the following sections we discuss potential explanations for this observed lack of sources.

3.4.2.1 Star formation suppression due to negative feedback

A popular mechanism previously suggested to explain a lack of LAEs around some quasars has been negative feedback from the quasar itself (Bañados et al., 2013, Mazzucchelli et al., 2017a, Morselli et al., 2014, Ota et al., 2018). In this scenario, the strong ionizing radiation from the quasar photoevaportates neutral hydrogen in its immediate vicinity, prohibiting gas condensation, and thus inhibiting star formation in galaxies which would normally be able to do so (Kim et al., 2009, Overzier et al., 2009). Our results are consistent with the expected scale of suppression in several works from the literature (e.g., Chen, 2020, Zhou et al., 2023), all suggesting that this effect should be within ~ 5 pMpc. We further quantify this by calculating the isotropic UV intensity in a sphere around the quasar, following Kashikawa et al. (2007), and determine the local flux density at different distances from the quasar via:

$$F_\nu^Q = \frac{L(\nu_L)}{4\pi r^2}, \tag{3.18}$$

where r is the distance from the quasar and $L(\nu_L)$ is the quasar luminosity at the Lyman limit. The later can be estimated by using the extinction-corrected rest-frame 1450 ÅAB magnitude:

$$L(\nu_L) = 4\pi D_L^2 f_\nu^0 10^{-0.4 m_{1450}} \left(\frac{912}{1450}\right)^{-\beta} \tag{3.19}$$

where D_L is the luminosity distance to the quasar, m_{1450} is the extinction-corrected rest-frame 1450 ÅAB magnitude, f_ν^0 is 3631 Jy, and β is the continuum slope (Fan et al., 2001). The 912/1450 term comes from the Lyman-break wavelength in angstroms and the the chosen rest-frame wavelength used to measure the continuum, often chosen to be rest-frame 1450 Å(see Mazzucchelli et al., 2017b).

Mazzucchelli et al. (2017b) measured the m_{1450} of VIK 2348–3054 to be 21.17 mag by extrapolating from the observed J-band magnitude. We also choose $\beta = -0.99$ following Kashikawa et al. (2007). Using Equations (3.18) and (3.19) we determine the local flux density at 2 pMpc and 5 pMpc to be:

$$F_\nu^Q(\nu_L; 2\text{pMpc}) = 9.0 \times 10^{-20} \text{erg cm}^{-2}\ \text{s}^{-1}\ \text{Hz}^{-1} \tag{3.20}$$

and

$$F_\nu^Q(\nu_L; 5\text{pMpc}) = 1.4 \times 10^{-20} \text{erg cm}^{-2}\ \text{s}^{-1}\ \text{Hz}^{-1}. \tag{3.21}$$

The isotropic UV intensity at the Lyman limit is then $J_{21} \sim 7$ and $J_{21} \sim 1$ at 2 pMpc and 5 pMpc respectively, where $J_{21} = J/10^{-21}$ erg cm^{-2} s^{-1} Hz^{-1} sr^{-1} and J is the UV intensity at the Lyman limit, determined by dividing the local flux density by 4π sr.

Several simulations suggest that the $J_{21} > 1$ is sufficient to completely inhibit star formations in haloes of mass below $10^9 M_\odot$ (Chen, 2020, Kashikawa et al., 2007, Thoul & Weinberg, 1996). Given this, and the values we determined for J_{21}, it is physically possible these LAEs have been suppressed within the quasar proximity zone—2.64 pMpc (Mazzucchelli et al., 2017b), shown by the shaded region in Figure 8—up to where we find the first LAE at 5 pMpc. However, for higher mass haloes, star formation wouldn't be suppressed; the heating caused by the ionizing radiation would be considerably less (an order of magnitude) than that of the high-mass collapsing gas cloud (Thoul & Weinberg, 1996). Therefore in the case of Lyman Break Galaxies (LBGs), which are generally accepted to have formed earlier and to be of larger mass than LAEs (Kashikawa et al., 2007) the effects of star formation suppression due to ionizing photons from the quasar should be smaller, if not entirely negligible. Given this, if the hole around the center is indeed caused by negative feedback, then an LBG search in the same field should reveal an overdensity of LBGs in general and populate the inner 5 pMpc around the quasar in particular. Observations of this field using the DECam y-band filter would allow us to perform this search (see §4.3 for a discussion on a recent LBG investigation around VIK J2348–3054 by Champagne et al., 2023).

Different quasar properties would influence the total observable suppression. This might explain the diversity of results within the literature, e.g., a more luminous quasar would be able to ionize higher mass haloes. Another factor would be the age of the quasar. Quasars need time to ionize their surroundings. The longer the quasar has been turned on, the larger the suppression radius. Finally, the covering factor of the quasar would directly influence how many ionizing photons could escape the AGN and affect the IGM. Therefore we would expect a relationship between covering factor and overdensity.

3.4.2.2 Cosmic variance

Another explanation for the lack of Ly-α emitters in the proximity of the quasar is cosmic variance; a chance arrangement of LAEs, without a physical cause. Indeed, this reason has been suggested by many studies to account for a lack of LAE concentrations around other high-redshift quasars (Bañados et al., 2013, Mazzucchelli et al., 2017a, Ota et al., 2018). The 1.2% probability of randomly finding the hole around the quasar suggests that this effect being caused by random chance is unlikely but still plausible.

Interestingly Chen (2020), using an adaptive refinement tree code on a suite of simulations, showed that the lack of faint galaxies due to suppression of star formation from quasars was a less important factor on the cumulative luminosity function than simple field-to-field variation. They determined this by searching for LAEs in random 1 pMpc radii spheres in simulations. Their results suggest that cosmic variance is an effect which needs to be considered seriously in this context. Accounting for cosmic variance robustly would require further comparisons, on similar depths and FoVs, to other blank fields as well as wider field of view observations of other quasar fields. In contrast to star formation suppression, LBGs would be expected to show a similar pattern as LAEs around VIK J2348–3054 if the observed structure is a result of cosmic variance.

3.4.2.3 Other possible physical mechanisms

The lack of central LAEs near the quasar might be physically driven by processes other than star formation suppression by the quasar.

A merging scenario was suggested by Bañados et al. (2013). In this model, the central quasar obtains sufficient mass through hierarchical mergers with surrounding haloes, which explains how high-redshift quasars are able to accrete enough mass so quickly and, at the same time, explains the apparent lack of the LAEs in the nearby vicinity as they would have merged with the host galaxy of the quasar.

Willott et al. (2005), Kim et al. (2009), and Mazzucchelli et al. (2017a), raised the possibility that candidates around the quasar might be dust obscured, thereby resulting in non-detections. However, explaining our results would require a gradient in the amount of dust as a function of the distance to the quasar, which seems unlikely. Submm interferometric surveys within the inner 5 pMpc might be able to confirm or deny this effect. However, mapping such a large area with, e.g., ALMA, would be observationally expensive. For example, ALMA observations have been taken of VIK J2348–3054 by Venemans et al. (2016), around a 0.13 armin^{-2} area, therefore only probing the immediate vicinity of the quasar, and found no companion galaxies.

Whilst these suggested mechanisms may be reasonable to explain the results of individual observations, they fail to account for the breadth of results throughout the literature—underdensities, field-densities, and an overdensities. Considering this, we conclude that negative feedback is the most likely explanation of the observed results.

3.4.3 Comparison to other studies

The varying results throughout the literature have been difficult to constrain and many explanations have been given for the scatter. We summarize the results of previous studies in Figure 12, where we found 20 high-redshift quasars in the literature that were searched for either LAEs or LBGs in order to trace an overdensity using imaging and color-selection. In this section, we try and put our results into context by comparing the observational properties of previous studies, in particular, how the field of view relates to the current literature, and comparing LBG searches to LAE searches.

Of the 20 quasars only six were searched for LAE overdensities. And of these six observations, none found overdensities. Furthermore there were no multiple LAE searches done on any of these quasars, meaning that only six LAE searches were done in total (Bañados et al., 2013, Goto et al., 2017, Kikuta et al., 2017, Mazzucchelli et al., 2017a, Ota et al., 2018). On the other hand, 16 of the quasars had LBG surveys done. Some quasars were studied multiple times by different groups. In total there were 24 LBG searches done, of which, 16 (67%) found overdensities whilst 8 (33%) did not. The fact that many LAE searches don't detect an overdensities, whilst at the same time, most LBG searches do, suggests that quasars may be ionizing their environments. As we mentioned previously, the younger, lower mass LAEs would be more affected than the older, higher mass LBGs. Therefore, we would expect to find less overdensities when looking for LAEs. Alternatively, narrowband imaging might not have enough sensitivity for these equivalent widths.

Before this work, only two quasars had both LAEs and LBGs searches done: VIK J0305–3150 and CFHQS J2329–0301. Ota et al. (2018) performed both a LBG and LAE on VIK J0305–3150 and found, at low masses, a slight overdensity of LBGs and an underdensity of LAEs. Later, Champagne et al. (2023) reported a massive overdensity of LBGs very near the quasar. Whilst narrowband searches for LAEs arround the quasar have resulted in non-detections, spectroscopic observations, in particular with MUSE on the Very Large Telescope, identified a LAE very near to the quasar (Farina et al., 2017). Recently, James Webb Space Telescope (JWST) slitless spectroscopy has identified 10 [OIII] emitting galaxies, which trace a filamentary structure around this quasar (Wang et al., 2023). These results highlight the importance that spectroscopic follow up can play in determining overdensities.

Utsumi et al. (2010) and Goto et al. (2017) both observed CFHQS J2329–0301 for LBGs and LAEs respectively, with Subaru/Suprime-Cam. Once again, the quasar had an overdensity of LBGs and an underdensity of LAEs.

Recently, Champagne et al. (2023) performed an LBG search around VIK J2348–3054 using the Advanced Camera for Surveys (ACS) onboard the Hubble Space Telescope (HST). Whilst they claim no LBG enhancement, they still find 10 LBG candidates within 0.3 pMpc, well within the quasar proximity zone. This is in stark contrast to our own observations of VIK J2348–3054, where we don't find any LAE over a much larger area. Once again, the lack of LAE and the detection of LBGs is expected, further hinting at star formation suppression.

To date, this study is the only one which has found an overdensity of LAEs around a high-redshift quasar ($z > 5$) using the narrowband search technique. At the same time, this is the largest area ever searched for either LBGs or LAEs (see the solid purple star in Figure 12). Moreover, had we observed VIK J2348–3054 with any other observational set up, on any of the other telescopes that were used in previous observations, we would not have detected an overdensity. This would seem to suggest that previous LAE non detection might have not been probing a large enough area, and wider FoV studies would possibly have revealed overdense regions.

3.5 Summary and Conclusion

In this paper we aimed to address important observational factors we believe have influenced previous studies which searched for overdensities around high-redshift quasars; we searched for LAEs over an enormous field of view, centered on a quasar with a confirmed [CII] redshift. And in doing so, we hoped to answer whether or not quasars live in overdense environments as has been predicted by simulations. This is the largest FoV searched for LAE or LBGs around a high-redshift quasar to date.

We found 38 LAE candidates around VIK J2348–3054 and applied our same selection criteria to the CDFS images for comparison. After degrading the CDFS data to match our shallower depths, we found only two LAE candidates. Adjusting for the differences in the usable areas of both fields, this implies that VIK J2348–3054 resides in an environment that is overdense by a factor of $\delta = 10^{+5.3}_{-5.9}$. The space density of our candidates also sit well above the $z \sim 7$ luminosity function of Hu et al. (2019) by a factor of $\delta = 14 \pm 3$, further supporting the presence of a large overdensity.

Interestingly, we identified a distinct lack of LAEs in the immediate vicinity around the quasar itself. Assuming that the surface density at distances further than 75 cMpc (Overzier et al., 2009) as representative for the field, we find that the lack of LAEs withing 5.15 pMpc of the quasar has a probability of only 1.2% of occurring by chance, which is not enough to exclude cosmic variance as a cause. However, given that the

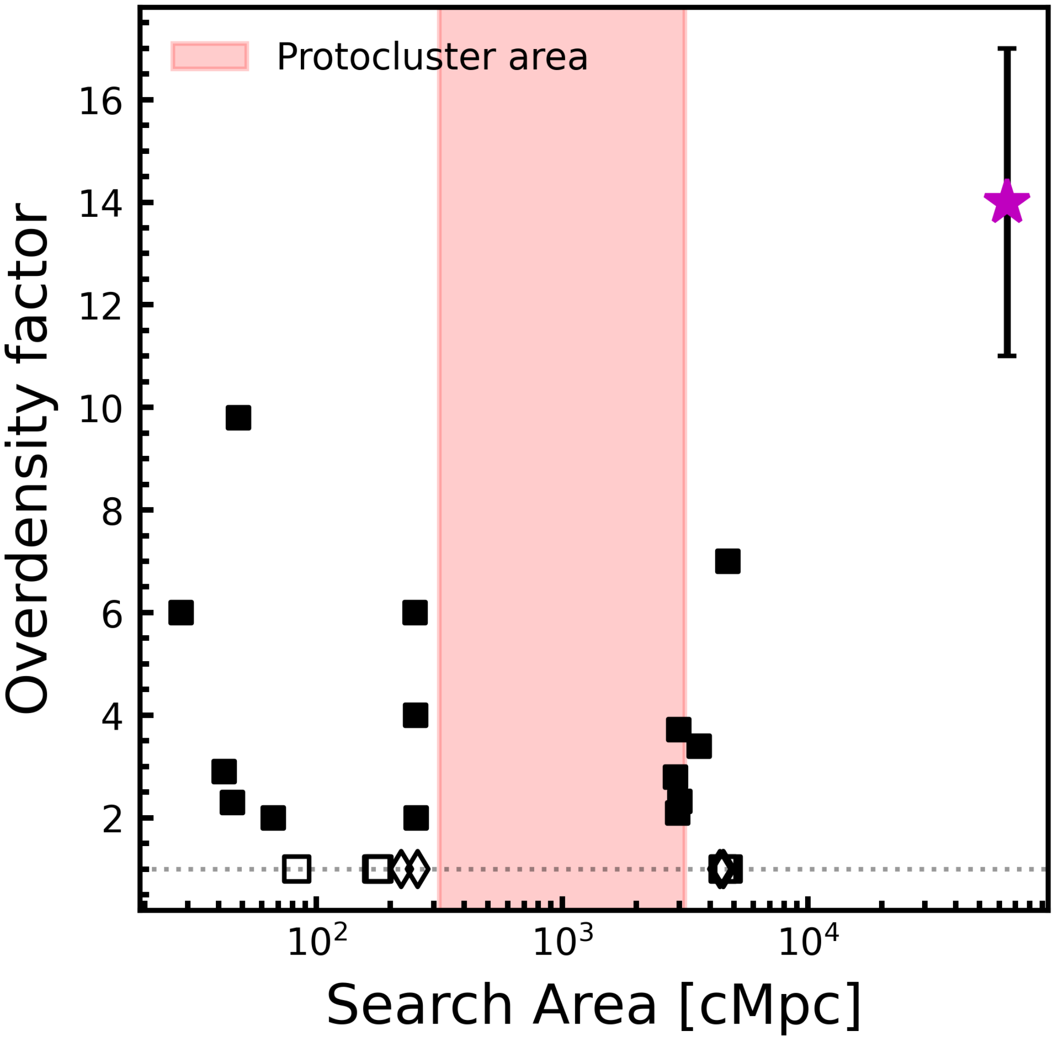

FIGURE 12: Summary plot of the various studies and results of looking for LAEs and LBGs around high-redshift quasars. Circles are Lyman-break searches, diamonds are Ly-α studies. Filled in values indicate that an overdensity was found, whilst not filled in represents that no overdensity was found.

underdensity is centerd on the quasar itself, we take this to be a conservative estimate and suggest that this suppression is more likely due to a physical mechanism associated with the quasar, in particular, ionizing radiation which is inhibiting star formation in nearby (< 5 pMpc) galaxies. We calculate the isotropic UV intensity at the Lyman limit at 2 pMpc and 5 pMpc for VIK J2348–3054 and show that this would be sufficient to suppress star formation in low mass galaxies such as LAEs but wouldn't be enough to suppress it in larger galaxies like LBGs. It is therefore interesting that a recent small-FoV search for LBGs around VIK J2348–3054 found 10 LBG candidates within 0.3 pMpc Champagne et al. (2023).

The spread of results we see within the literature could be from a variety of factors. If the quasar is indeed suppressing star formation in its nearby vicinity then that suppression would be dependent on the luminosity, age, and covering factor of the quasar, and the combination of one or any combination of these factors could induce a spread of results. Alternatively, smaller FoV studies may be dominated by cosmic variance.

Follow up observations of this field will be essential; LBG searches in particular, as well as spectroscopic follow up will help differentiate between cosmic variance and suppression of star formation. An LBG search could be conducted on these large scales with just a y-band observation.

This work has highlighted the importance of large-FoV studies and how not probing a large enough area might result in false non-detections of overdensities. It is therefore critical to perform large-FoV follow up surveys of other quasar fields, not only to account for the small FoV of other surveys, but also to investigate the role that cosmic variance has on these kinds of surveys. It is also clear that future searches will require consistent methodologies to observationally confirm whether or not quasars live in overdense regions. Therefore, a large-FoV campaign to observe multiple high-redshift quasars would be invaluable.

Chapter 4

What's next?

When I started this Ph.D. in 2020, there were only rumours that the James Webb Space Telescope (JWST) would be launched in the next couple years. Given that we had been hearing these same rumours for the last twenty years, nobody was inclined to believe them. However, on Christmas day 2021, JWST was launched successfully and has fundamentally changed the type of science we can do at high redshifts. It has become an essential tool to study the early Universe. There have also been several large ALMA projects which have emerged over the last couple years which will undoubtedly contribute towards future work in this field.

In this section I discuss how new projects and facilities will build upon the work that I have presented and mention possible follow up observations that will expand the work done in this thesis.

4.1 [CII] Haloes and the ISM of Galaxies at Cosmic Dawn

Hz7 (discussed in Chapter 2) is just one of a sample of main-sequence galaxies. Other individual targets, such as COS-2987030247 Posses et al. (2023) and HZ3 (Posses et. al., in prep) have also been observed. But we need a larger sample of [CII] observations around other main sequence galaxies in order to make any robust claims about 1) if these haloes are a ubiquitous stage of galaxy evolution, and 2) what physical mechanisms drive their development. Fortunately, a large ALMA program—[CII] resolved ISM in star-forming galaxies with ALMA (CRISTAL)—has begun a campaign to observe the [CII] line and dust continuum of 19 main-sequence, star forming galaxies at $z \sim 4-5$. This will undoubtedly begin to answer the question of whether or not [CII] haloes are a ubiquitous amongst normal galaxies at these redshifts. However, the true strength of this program will come from complimentary restframe UV and IR observations.

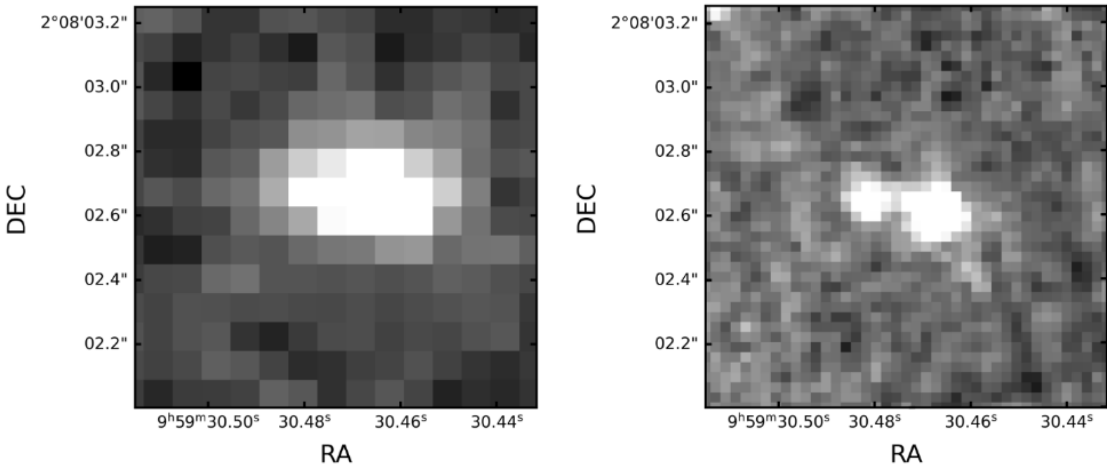

Figure 1: Comparison between an HST F105W image (left) and a JWST F115W image (right) of Hz7.

For example, consider the case of Hz7; one of the main conclusions from Lambert et al. (2023) was that the Hz7 system was actually a late-stage merger. And this, as apposed to outflows (though these may not be mutually exclusive), is the physical reason behind [CII] haloes. HST imaging of the system was unable to determine if this was indeed the case. However, JWST imaging of the system, as part of the COSMOS-Web (PID: 1727) Cycle 1 program, has been able to definitively show that Hz7 is comprised of two, individual sources. Figure 1 shows the comparison between the HST imaging and JWST imaging of Hz7.

What's more, Hz7 is not the only target which has been observed by the COSMOS-Web project (Casey et al., 2023). There is significant overlap between the CRISTAL target list and the these JWST observations. Future results of a large sample of [CII], JWST, and HST imaging will not only explore how ubiquitous [CII] haloes are, but also discover the physical mechanism behind them. There has also been many new ALMA Cycle 10 proposals to explicitly search for [CII] emission around other galaxies, many of whom already have, or will have, JWST imaging. This is a perfect example of the combined power of ALMA and JWST and the kinds of exciting science that might arise because of it. Both can be used to study different aspects of high redshift galaxy evolution.

In a way, this Hz7 project acted as a pilot study, proving that not only can we directly detect [CII] haloes with ALMA, but we can probe their physical mechanisms too.

4.2 High-z quasars and their environments

Our results have demonstrated that there is a lot of work still required if we are to determine whether or not quasars, in the early universe, generally live in overdense environments. In particular, what we have shown is the importance of probing a large enough area; our overdensity was only possible because we implemented the largest area search of this kind. In particular, we have shown that DECam is an ideal instrument for this kind of work. I believe this study has opened the door to further DECam observations. One proposal that could already be considered is searching for LBGs around this same quasar field. Because we expect LAEs to be more affected by star formation suppression than LBGs (see the introduction of Chapter 3), an LBG search around VIK J2348-3054 would reveal an overdensity of LBGs within 5 pMpc of the quasar, if the void around VIK J2348-3054 is caused by negative feedback. Alternatively, if it is not, and the cause is due to cosmic variance (which our data does not rule out), then we would expect both the LBG and LAE on-sky distributions to match. We could perform a LBG search by observing this field in the y-band with DECam. This is a relatively cheap observation, considering that it only requires a single band observation, and the results would be far reaching.

Additionally, spectroscopic follow up of the LAE candidates, and LBG candidates if they were to be determined, would further solidify our main finding. This would be a lot more observationally expensive, however, it would confirm the central lack of LAEs, which would make the field of VIK J2348-3054 worthy of such an effort. In theory, confirmation of these redshifts could done with ALMA by identifying any [CII] gas around the LAE candidates.

Another important aspect that was highlighted by this project was the numerous methods, instruments, selection criteria, and various FoVs that have been used to determine overdensities around quasars. In fact, even the overdensity definition can vary from study to study. Such a spread of variables makes comparing one project to another difficult, and ultimately, diminishes the benefit of having a large sample of searches around high redshift quasars. Some level of normalization will need to take place in the future if we are to ever converge towards an answer.

Fortunately, a JWST Cycle 1 program, A SPectroscopic survey of biased halos In the Reionization Era (ASPIRE), will observe the environments around 25 Epoch of Reionization quasars using slitless spectroscopy. This will allow them to identify galaxies with H-α, H-β, and [OIII] emission lines, near the quasar. In other words, a uniform search around a large quasar sample. The results of this survey will be very interesting in light of the current tension in the literature. However, the FoV of view being searched around each quasar is nearly a 1000x times smaller in comparison to our own work, and, more importantly, in comparison to the expected size of a protocluster at these redshifts ($\sim$0.7 deg^2; $\sim$ 60 cMpc). ASPIRE will essentially probe galaxies within the proximity zone of the quasar. And whilst their results will undoubtedly become an important part of the ongoing discussion around high-z quasar environments, a campaign to study these sources over a large FoV will still be needed. Performing LAE searches for many different sources is difficult because each source would require a different narrowband, depending on their redshifts, but a large DECam survey, looking for LBGs around these quasars, is conceivable.

Looking for candidates around quasars is essential for exploring quasar environments. However, as important, is the need to constrain the quasar properties themselves. A JWST program to explore certain quasar properties, instead of focusing on their environments, would be interesting. As mentioned, if the quasar is influencing its environment, and therefore influencing the overdensity of companion galaxies, then we would expect to see a relationship between overdensity and quasar properties such as luminosity, lifetime, proximity zone, and torus covering fraction. In particular, the covering factor from the warm dust of these high redshift quasars can only be measured using the Mid-InfraRed Instrument (MIRI).

Exploring how the properties of the full sample of quasars relate to published overdensities is a crucial next step in trying to answer this question and would be an incredibly useful survery/catalog for any future work in this regard.

References

Abbott, T. M. C., Adamów, M., Aguena, M., et al. 2021, ApJS, 255, 20

Angulo, R. E., Springel, V., White, S. D. M., et al. 2012, MNRAS, 425, 2722

Appleton, P. N., Guillard, P., Boulanger, F., et al. 2013, ApJ, 777, 66

Bañados, E., Venemans, B., Walter, F., et al. 2013, ApJ, 773, 178

Balmaverde, B., Gilli, R., Mignoli, M., et al. 2017, A&A, 606, A23

Barisic, I., Faisst, A. L., Capak, P. L., et al. 2017, ApJ, 845, 41

Bertin, E., & Arnouts, S. 1996, A&AS, 117, 393

Béthermin, M., Fudamoto, Y., Ginolfi, M., et al. 2020, A&A, 643, A2

Bosman, S. E. I., Davies, F. B., Becker, G. D., et al. 2022, MNRAS, 514, 55

Bouwens, R. J., Illingworth, G., Ellis, R. S., et al. 2022a, ApJ, 931, 81

Bouwens, R. J., Smit, R., Schouws, S., et al. 2022b, ApJ, 931, 160

Bradley, L. D., Bouwens, R. J., Ford, H. C., et al. 2008, ApJ, 678, 647

Bruzual, G., & Charlot, S. 2003, MNRAS, 344, 1000

Capak, P. L., Riechers, D., Scoville, N. Z., et al. 2011, Nature, 470, 233

Capak, P. L., Carilli, C., Jones, G., et al. 2015, Nature, 522, 455

Carilli, C. L., & Walter, F. 2013, ARA&A, 51, 105

Carniani, S., Marconi, A., Biggs, A., et al. 2013, A&A, 559, A29

Carniani, S., Maiolino, R., Pallottini, A., et al. 2017, A&A, 605, A42

Carraro, R., Rodighiero, G., Cassata, P., et al. 2020, A&A, 642, A65

Casey, C. M. 2012, MNRAS, 425, 3094

Casey, C. M., Narayanan, D., & Cooray, A. 2014, , 541, 45

Casey, C. M., Kartaltepe, J. S., Drakos, N. E., et al. 2023, ApJ, 954, 31

Chambers, K. C., Magnier, E. A., Metcalfe, N., et al. 2016, arXiv e-prints, arXiv:1612.05560

Champagne, J. B., Casey, C. M., Finkelstein, S. L., et al. 2023, ApJ, 952, 99

Chen, H. 2020, ApJ, 893, 165

Costa, T., Sijacki, D., Trenti, M., & Haehnelt, M. G. 2014, MNRAS, 439, 2146

Czekala, I., Loomis, R. A., Teague, R., et al. 2021, ApJS, 257, 2

da Cunha, E., Groves, B., Walter, F., et al. 2013, ApJ, 766, 13

Daddi, E., Dickinson, M., Morrison, G., et al. 2007, ApJ, 670, 156

Dayal, P., & Ferrara, A. 2018, , 780, 1

Decarli, R., Walter, F., Venemans, B. P., et al. 2018, ApJ, 854, 97

Decarli, R., Mignoli, M., Gilli, R., et al. 2019, A&A, 631, L10

Díaz-Santos, T., Armus, L., Charmandaris, V., et al. 2013, ApJ, 774, 68

—. 2017, ApJ, 846, 32

Díaz-Santos, T., Assef, R. J., Eisenhardt, P. R. M., et al. 2021, A&A, 654, A37

Dressler, A. 1980, ApJ, 236, 351

Dressler, A., Oemler, A., Gladders, M. G., et al. 2009, ApJL, 699, L130

Dunlop, J. S. 2013, in Astrophysics and Space Science Library, Vol. 396, The First Galaxies, ed. T. Wiklind, B. Mobasher, & V. Bromm, 223

Eilers, A.-C., Simcoe, R. A., Yue, M., et al. 2023, ApJ, 950, 68

Ellis, R., Santos, M. R., Kneib, J.-P., & Kuijken, K. 2001, ApJL, 560, L119

Ellis, R. S., McLure, R. J., Dunlop, J. S., et al. 2013, ApJL, 763, L7

Endsley, R., Stark, D. P., Lyu, J., et al. 2022, arXiv e-prints, arXiv:2206.00018

Faisst, A. L., Yan, L., Béthermin, M., et al. 2022, Universe, 8, 314

Fan, X., Bañados, E., & Simcoe, R. A. 2023, ARA&A, 61, 373

Fan, X., Strauss, M. A., Richards, G. T., et al. 2001, AJ, 121, 31

Fan, X., Strauss, M. A., Becker, R. H., et al. 2006, AJ, 132, 117

Farina, E. P., Venemans, B. P., Decarli, R., et al. 2017, ApJ, 848, 78

Farina, E. P., Schindler, J.-T., Walter, F., et al. 2022, ApJ, 941, 106

Foreman-Mackey, D., Hogg, D. W., Lang, D., & Goodman, J. 2013, PASP, 125, 306

Fujimoto, S., Ouchi, M., Ferrara, A., et al. 2019, ApJ, 887, 107

Fujimoto, S., Silverman, J. D., Bethermin, M., et al. 2020, ApJ, 900, 1

Gaia Collaboration, Brown, A. G. A., Vallenari, A., et al. 2018a, A&A, 616, A1

—. 2018b, A&A, 616, A1

Gallerani, S., Neri, R., Maiolino, R., et al. 2012, A&A, 543, A114

García-Vergara, C., Hennawi, J. F., Barrientos, L. F., & Rix, H.-W. 2017, ApJ, 848, 7

Gavazzi, R., Treu, T., Marshall, P. J., Brault, F., & Ruff, A. 2012, ApJ, 761, 170

Gehrels, N. 1986, ApJ, 303, 336

Giavalisco, M. 2002, Annual Review of Astronomy and Astrophysics, 40, 579

Ginolfi, M., Jones, G. C., Béthermin, M., et al. 2020a, A&A, 633, A90

—. 2020b, A&A, 643, A7

Gomez, H. L., Baes, M., Cortese, L., et al. 2010, A&A, 518, L45

Goto, T., Utsumi, Y., Kikuta, S., et al. 2017, MNRAS, 470, L117

Gottlöber, S., Klypin, A., & Kravtsov, A. V. 2001, ApJ, 546, 223

Hani, M. H., Sparre, M., Ellison, S. L., Torrey, P., & Vogelsberger, M. 2018, MNRAS, 475, 1160

Herrera-Camus, R., Förster Schreiber, N., Genzel, R., et al. 2021, A&A, 649, A31

Hodge, J. A., & da Cunha, E. 2020, Royal Society Open Science, 7, 200556

Hu, W., Wang, J., Zheng, Z.-Y., et al. 2019, ApJ, 886, 90

Husband, K., Bremer, M. N., Stanway, E. R., et al. 2013, MNRAS, 432, 2869

Ilbert, O., McCracken, H. J., Le Fèvre, O., et al. 2013, A&A, 556, A55

Inayoshi, K., Visbal, E., & Haiman, Z. 2020, ARA&A, 58, 27

Jorsater, S., & van Moorsel, G. A. 1995, AJ, 110, 2037

Kampczyk, P., Lilly, S. J., de Ravel, L., et al. 2013, ApJ, 762, 43

Kashikawa, N., Kitayama, T., Doi, M., et al. 2007, ApJ, 663, 765

Kennicutt, Robert C., J. 1998, ARA&A, 36, 189

Kennicutt, R. C., & Evans, N. J. 2012, ARA&A, 50, 531

Khostovan, A. A., Malhotra, S., Rhoads, J. E., et al. 2020, MNRAS, 493, 3966

Kikuta, S., Imanishi, M., Matsuoka, Y., et al. 2017, ApJ, 841, 128

Kim, S., Stiavelli, M., Trenti, M., et al. 2009, ApJ, 695, 809

Lambert, T. S., Posses, A., Aravena, M., et al. 2023, MNRAS, 518, 3183

Landy, S. D., & Szalay, A. S. 1993, ApJ, 412, 64

Le Fèvre, O., Béthermin, M., Faisst, A., et al. 2020, A&A, 643, A1

Leauthaud, A., Massey, R., Kneib, J.-P., et al. 2007, ApJS, 172, 219

Leroy, A. K., Walter, F., Brinks, E., et al. 2008, AJ, 136, 2782

Linzer, N., & Steinhardt, C. 2020, in American Astronomical Society Meeting Abstracts, Vol. 235, American Astronomical Society Meeting Abstracts #235, 207.11

Livermore, R. C., Finkelstein, S. L., & Lotz, J. M. 2017, ApJ, 835, 113

Madau, P. 1995, ApJ, 441, 18

Madau, P., & Dickinson, M. 2014a, ARA&A, 52, 415

—. 2014b, ARA&A, 52, 415

Maiolino, R., Carniani, S., Fontana, A., et al. 2015, MNRAS, 452, 54

Massa, D., Gordon, K. D., & Fitzpatrick, E. L. 2022, ApJ, 925, 19

Matthee, J., Sobral, D., Santos, S., et al. 2015, MNRAS, 451, 400

Matthee, J., Sobral, D., Boogaard, L. A., et al. 2019, ApJ, 881, 124

Mazzucchelli, C., Bañados, E., Decarli, R., et al. 2017a, ApJ, 834, 83

Mazzucchelli, C., Bañados, E., Venemans, B. P., et al. 2017b, ApJ, 849, 91

Mazzucchelli, C., Bischetti, M., D'Odorico, V., et al. 2023, A&A, 676, A71

McMullin, J. P., Waters, B., Schiebel, D., Young, W., & Golap, K. 2007, in Astronomical Society of the Pacific Conference Series, Vol. 376, Astronomical Data Analysis Software and Systems XVI, ed. R. A. Shaw, F. Hill, & D. J. Bell, 127

Mignoli, M., Gilli, R., Decarli, R., et al. 2020, A&A, 642, L1

Morselli, L., Mignoli, M., Gilli, R., et al. 2014, A&A, 568, A1

Mosenkov, A. V., Baes, M., Bianchi, S., et al. 2019, A&A, 622, A132

Muldrew, S. I., Hatch, N. A., & Cooke, E. A. 2015, Monthly Notices of the Royal Astronomical Society, 452, 2528

Nelson, D., Genel, S., Vogelsberger, M., et al. 2015, MNRAS, 448, 59

Obreschkow, D., Croton, D., De Lucia, G., Khochfar, S., & Rawlings, S. 2009, ApJ, 698, 1467

Oesch, P. A., Bouwens, R. J., Illingworth, G. D., Labbé, I., & Stefanon, M. 2018, ApJ, 855, 105

Oesch, P. A., Brammer, G., van Dokkum, P. G., et al. 2016, ApJ, 819, 129

Osterbrock, D. E. 1989, Astrophysics of gaseous nebulae and active galactic nuclei

Ota, K., Walter, F., Ohta, K., et al. 2014, ApJ, 792, 34

Ota, K., Venemans, B. P., Taniguchi, Y., et al. 2018, ApJ, 856, 109

Ouchi, M., Ono, Y., & Shibuya, T. 2020, ARA&A, 58, 617

Overzier, R. A., Guo, Q., Kauffmann, G., et al. 2009, MNRAS, 394, 577

Pallottini, A., Ferrara, A., Gallerani, S., Salvadori, S., & D'Odorico, V. 2014, MNRAS, 440, 2498

Pimbblet, K. A., Smail, I., Kodama, T., et al. 2002, MNRAS, 331, 333

Pizzati, E., Ferrara, A., Pallottini, A., et al. 2020, MNRAS, 495, 160

Posses, A. C., Aravena, M., González-López, J., et al. 2023, A&A, 669, A46

Postman, M., & Geller, M. J. 1984, ApJ, 281, 95

Rodriguez-Gomez, V., Genel, S., Vogelsberger, M., et al. 2015, MNRAS, 449, 49

Romano, M., Cassata, P., Morselli, L., et al. 2021, A&A, 653, A111

Schaerer, D., Ginolfi, M., Béthermin, M., et al. 2020, A&A, 643, A3

Schindler, J.-T., Farina, E. P., Bañados, E., et al. 2020, ApJ, 905, 51

Schouws, S., Bouwens, R., Smit, R., et al. 2022, arXiv e-prints, arXiv:2202.04080

Schruba, A., Leroy, A. K., Walter, F., et al. 2011, AJ, 142, 37

Scoville, N., Aussel, H., Brusa, M., et al. 2007, ApJJS, 172, 1

Scoville, N., Lee, N., Vanden Bout, P., et al. 2017, ApJ, 837, 150

Shapley, A. E. 2011, Annual Review of Astronomy and Astrophysics, 49, 525

Shibuya, T., Ouchi, M., & Harikane, Y. 2015, ApJS, 219, 15

Silverman, J. D., Daddi, E., Rodighiero, G., et al. 2015, ApJL, 812, L23

Simpson, C., Mortlock, D., Warren, S., et al. 2014, MNRAS, 442, 3454

Speagle, J. S., Steinhardt, C. L., Capak, P. L., & Silverman, J. D. 2014, ApJS, 214, 15

Stark, D. P. 2016, ARA&A, 54, 761

Stefanon, M., Bouwens, R. J., Labbé, I., et al. 2021, ApJ, 922, 29

—. 2022, ApJ, 927, 48

Steinhardt, C. L., Jespersen, C. K., & Linzer, N. B. 2021, ApJ, 923, 8

Stiavelli, M., Djorgovski, S. G., Pavlovsky, C., et al. 2005, ApJL, 622, L1

Thoul, A. A., & Weinberg, D. H. 1996, ApJ, 465, 608

Tumlinson, J., Peeples, M. S., & Werk, J. K. 2017, Annual Review of Astronomy and Astrophysics, 55, 389

Utsumi, Y., Goto, T., Kashikawa, N., et al. 2010, ApJ, 721, 1680

Valdes, F., Gruendl, R., & DES Project. 2014, in Astronomical Society of the Pacific Conference Series, Vol. 485, Astronomical Data Analysis Software and Systems XXIII, ed. N. Manset & P. Forshay, 379

Venemans, B. P., McMahon, R. G., Warren, S. J., et al. 2007, MNRAS, 376, L76

Venemans, B. P., Walter, F., Zschaechner, L., et al. 2016, ApJ, 816, 37

Venemans, B. P., Findlay, J. R., Sutherland, W. J., et al. 2013, ApJ, 779, 24

Venemans, B. P., Bañados, E., Decarli, R., et al. 2015, ApJL, 801, L11

Vito, F., Brandt, W. N., Yang, G., et al. 2018, MNRAS, 473, 2378

Volonteri, M. 2012, Science, 337, 544

Walter, F., Carilli, C., & Daddi, E. 2010, Reviews in Modern Astronomy, 22, 167

Walter, F., Riechers, D., Cox, P., et al. 2009, Nature, 457, 699

Wang, F., Yang, J., Fan, X., et al. 2021, ApJL, 907, L1

Wang, F., Yang, J., Hennawi, J. F., et al. 2023, ApJL, 951, L4

Wang, R., Wagg, J., Carilli, C. L., et al. 2013, ApJ, 773, 44

Willott, C. J., Percival, W. J., McLure, R. J., et al. 2005, ApJ, 626, 657

Willott, C. J., Delorme, P., Reylé, C., et al. 2010, AJ, 139, 906

Wold, I. G. B., Kawinwanichakij, L., Stevans, M. L., et al. 2019a, ApJS, 240, 5

—. 2019b, ApJS, 240, 5

Wold, I. G. B., Malhotra, S., Rhoads, J., et al. 2022, ApJ, 927, 36

Yang, J., Wang, F., Fan, X., et al. 2023, ApJL, 951, L5

Zewdie, D., Assef, R. J., Mazzucchelli, C., et al. 2023, A&A, 677, A54

Zheng, W., Overzier, R. A. asnd Bouwens, R. J., White, R. L., et al. 2006, ApJ, 640, 574

Zheng, W., Postman, M., Zitrin, A., et al. 2012, Nature, 489, 406

Zheng, Z.-Y., Rhoads, J. E., Wang, J.-X., et al. 2019, PASP, 131, 074502

Zhou, Y., Chen, H., Di Matteo, T., et al. 2023, arXiv e-prints, arXiv:2309.11571